Experimental and numerical study on the thermocline behavior of packed-bed storage tank with sensible fillers

Baoshan Xie, Nicolas Baudin, Jérôme Soto, Yilin Fan, Lingai Luo

Experimental and numerical study on the thermocline behavior of packed-bed storage tank with sensible fillers

Baoshan XIE[a], Nicolas BAUDIN[a], Jérôme SOTO[a,b], Yilin FAN[a], Lingai LUO[a,*]

[a] *Nantes Université, CNRS, Laboratoire de Thermique et énergie de Nantes, LTeN, UMR 6607, 44000 Nantes, France*

[b] *Institut Catholique d'Arts et Métiers de Nantes, 35 avenue du Champ de Manœuvres, 44470 Carquefou, France*

Abstract: Packed-bed thermocline tank with sensible fillers is a cost-effective option for thermal energy storage (TES). In real charging and discharging, the thermocline stability is disturbed and thermocline expansion occurs due to various factors, leading to the decreased global performances of storage tank. The purpose of this work is to experimentally and numerically study the impact of inlet configuration and insulation on the thermocline expansion in a lab-scale tank under various operating parameters. Firstly, a DC-3P model considering the wall effect and heat loss is developed and validated by experimental results, capable of precisely predicting the performance of storage tank under the tested conditions. Especially, the temperature difference between the fluid and solid filler center is detected both in experiments and in modeling, indicating the existence of temperature gradient inside large solid particles. Results also show that the injecting flow causes the radial temperature non-uniformity and thermocline expansion at the near-entrance region of the tank, but its effect on the global performance of the storage tank is rather limited. Good insulation of the tank could reduce the thermocline thickness by about 20%, and increase the energy efficiency and the capacity ratio by 5-7% and 3-5%, respectively.

Keywords: Thermal energy storage; Packed-bed thermocline; Sensible fillers; Flow diffuser; Insulation

* Corresponding author
E-mail address: lingai.luo@univ-nantes.fr (L. LUO)

Nomenclature

A	Superficial area (m^2)
Bi	Biot number, $Bi=h\cdot(V/A)/\lambda$
C_p	Specific heat capacity (J kg^{-1} K^{-1})
C_{ratio}	Capacity ratio
D_p	Diameter of particle (m)
D_{tank}	Diameter of tank (m)
E	Energy (J)
g	Acceleration due to gravity (m s^{-2})
Gr	Grashof number, $Gr=g\cdot\beta\cdot H^3\cdot\Delta T/\nu^2$
h	Heat transfer coefficient (W m^{-2} K^{-1})
H	Height of tank (m)
L	Layer thickness (m)
$\dot{m}$	Mass flow rate (kg s^{-1})
ΔP	Pressure drop (Pa)
Pe	Péclet number, $Pe=D_p\cdot u_{sup}/\alpha$
Pr	Prandtl number, $Pr=C_{p,f}\cdot\mu_f/\lambda_f$
r_p	Radial coordinate of sphere
r	Radial coordinate of tank
Ra	Rayleigh number, $Ra= Gr\cdot Pr$
Re	Reynolds number for particle, $Re=(\rho_f\cdot D_p\cdot u_{sup})/\mu_f$
R_{int}	Internal radius of tank (m)
R_{mid}	Middle radius of tank (m)
R_{ext}	External radius of tank (m)
t	Time (s)
T	Temperature (K)
T_C	Coldest operation temperature (K)
T_H	Highest operation temperature (K)
T_{in}	Fluid inlet temperature (K)
T_{out}	Fluid outlet temperature (K)
T_o	Reference temperature (K)
T^A	Radial temperature of A position
T^B	Radial temperature of B position
T^C	Radial temperature of C position
u	Interstitial fluid velocity (m s^{-1}), $u=\dot{m}/(\rho_f\cdot\varepsilon\cdot\pi\cdot R^2_{int})$
u_{sup}	Superficial fluid velocity (m s^{-1}), $u_{sup}=u\cdot\varepsilon$
V	Volume (m^3)
$\dot{V}_f$	Volumetric flow rate (m^3 s^{-1})
z	Axial coordinate of tank
f_r	Non-uniformity factor

Greek symbols

α	Thermal diffusivity (m^2 s^{-1}), $\alpha= \lambda/(\rho\cdot C_p)$
λ	Thermal conductivity (W m^{-1} K^{-1})
ε	Porosity
μ	Dynamic viscosity (Pa s)
ϑ	Uncertainty
ρ	Density (kg m^{-3})
ϵ	Emissivity
β	Expansion coefficient of air (K^{-1})
η	Energy efficiency
ν	Kinematic viscosity (m^2 s^{-1})
σ	Stefan-Boltzmann constant, $=5.67\times10^{-8}$ $W\cdot m^{-2}\cdot K^{-4}$
Φ	Diameter (m)
θ	Outlet temperature threshold coefficient

Subscripts

amb	Ambient
b	Packed bed region of inner tank diameter
ch	Charging
dis	Discharging
eff	Effective value
ext	External surface of tank
f	Fluid
in	Inlet
int	Internal surface of tank
max	Maximum
out	Outlet
p	Particle
rad	Radiative
s	Solid
sf	Solid-to-fluid phase
w	Wall

1. Introduction

The yearly growing in energy demand worldwide and the carbon dioxide emission in 2021 have reached about 4.6% and 5%, respectively [1]. As a promising alternative to traditional fossil sources, renewable energies get great attention to mitigate climate change and environmental pollution concerns. In 2020, renewable energy represented 22.1 % of energy consumed in European countries and is still significantly expanding to meet the goal of European Green Deal by 2050 [2,3]. Nevertheless, the intermittent and fluctuating nature of these renewable sources (e.g., solar energy) calls for the development and deployment of efficient thermal energy storage (TES) techniques to improve the system's flexibility and dispatchability [4–6]. For example, more than 70% of the concentrated solar power (CSP) plants under construction have combined with TES system and this ratio is still increasing for future more powerful plants [7]. According to the storage mechanism, TES systems can be classified into sensible [8], latent [9], and thermochemical [10] heat categories. Among them, sensible heat storage is currently the most mature and commonly-used technology for various applications.

Thermocline-based TES technology involves a type of single-tank storage system where hot and cold heat transfer fluids (HTF) are both stored in the same tank [11]. The thermocline or thermal stratification zone with a temperature gradient is formed around the interface between the hot and cold fluids. It periodically moves up/down in the axial direction during the charging/discharging operations. Compared to the conventional two-tank TES system, the thermocline concept is a more competitive option with about 37% cost reduction, by cutting the needed two tanks into one and by using the cheaper sensible fillers (e.g., rocks or concretes) to substitute the amount of some expansive liquid HTF used as storage media (e.g., oil or molten salt) [12]. For all these reasons, the sensible-heat thermocline packed-bed (SHTPB) TES system has become a research focus in recent years.

In theory, the thermocline stability and thickness affects the SHTPB system's performance: a higher level of thermal stratification or a thinner thermocline zone means higher energy and exergy efficiencies [13,14]. Nevertheless, the thermal stratification tends to become unstable and expanded over dynamic and cycling operations. This thermocline degradation, or decay, can be due to many factors [15,16]. On

one hand, the low heat transfer rate between HTF and solid fillers or the heat diffusion, inside the HTF, the solid media, or the wall phases would result in the expanded thermocline thickness in the axial direction [17]. On the other hand, the flow injection, the heat loss to the environment, and the wall properties would cause the non-uniform radial temperature distribution inside the tank, lowering the thermocline stability and increasing the thickness [18].

Uniform radial flow velocity and temperature profiles are usually assumed in one-dimensional (1D) models (e.g., Schumann's model) for modeling SHTPB systems due to the flow homogenizing effect of the porous fillers [19]. The necessity of additional flow diffuser instead of inlet port in packed-bed storage tanks to guarantee the good and stable thermal stratification is controversy in early stages. Study was focused on installing special types of flow diffuser in SHTPB tanks to effectively utilize the bed domain [20]. Later, Bruch et al. [21] experimentally observed that there was no significant inhomogeneity of radial temperature in a SHTPB tank without diffuser. The authors stated that the 1D heat transfer model was adequate for the configuration where tank height to diameter aspect ratio H/D_{tank} =3. Yin et al. [22,23] also experimentally tested a near-tube tank (H/D_{tank} =5) and showed that the porous fillers could help to maintain the HTF as an ideal plug flow pattern. However, depending on different filler configurations and heat transfer mechanisms, the impact of injecting flow on the thermal performance is different. For example, Reddy and Pradeep [24] numerically observed that the radial non-uniform temperature distribution in their SHTPB tank (H/D_{tank} =4) is negligible in laminar flow owing to the porous packed bed working as flow distributor, but not in turbulent condition. Wang et al. [25] simulated a flow annular diffuser (80% annular area) at the inlet of a SHTPB tank (H/D_{tank} =1/3) and found that the non-uniform radial flow has a limited influence on output energy but it could affect the interstitial heat transfer, thus improving the thermal performance. Recently, Vannerem et al. [26] analyzed this problem by comparing three types of baffle-type flow diffusers under different flow rates. It has been reported that the solid filler could act as a natural distributor and the fluid distribution at the inlet did not impact the global storage performance due to the flow being restricted to a small fraction of the packed bed in their SHTPB tank (H/D_{tank} =2). In brief, more investigations are still needed to show from what distance to the inlet such radial temperature gradient can be eliminated by the porous

bed with different packing properties (e.g., particle size, porosity etc.), and to further clarify the relation between the thermocline expansion due to the injecting fluid flow and the global thermal performance reduction of the SHTPB tank.

The heat losses and associated wall impact are another influencing factor on the radial temperature distribution of SHTPB tank. Early studies [27,28] reported the existence of radial temperature gradient for about 30-40% of the tank radius due to the heat loss, leading to the higher centerline temperature than that in near-wall region. This radial temperature gradient cannot be taken in account in the 1D model and will cause the smaller amount of energy stored in the SHTPB tank than predicted [18,29]. Hoffmann et al. [15,30] reported that the heat losses would lead to the unstable thermocline, reduced output power, and decreased outlet temperature. Xie et al. [31] have developed adapted transient models to systematically explore the wall impact on the dynamic thermocline behavior of the SHTPB tanks by including the wall and insulation heat capacity in the governing equations. The most influencing factors have also been identified to provide useful design guidelines. Nevertheless, the experimental investigations of a SHTPB tank under two extreme conditions, with or without insulation, on the thermocline expansion are still insufficient, especially for tanks operated with storage temperature range less than <100 °C. **Table *1*** lists main experimental investigations using sensible fillers reported in the literature.

Therefore, this work is devoted to investigating the dynamic thermocline behaviors of the packed-bed system under the impacts of inlet configuration and insulation in different operational conditions, including HTF flow rate, inlet temperature, filler particle size, etc.. At first, a numerical dispersion-concentric three-phase phase (DC-3P) model was developed and its applicable range was determined in view of model validation. Then, to assess the influences of radial temperature non-uniformity due to the injecting flow and heat loss, an experimental lab-scale tank of SHTPB was fabricated and tested under controlled conditions. Three inlet configurations (using a structured inlet diffuser) and two insulation configurations were compared. In the end, the effects of heat diffusion in fluid and solid phases and the heat convection between the HTF and solid fillers on the axial thermocline expansion are further discussed.

This work is fitted to small flow rates (Reynolds numbers, Re<15), relatively large particle size (sphere Biot number, Bi_s>0.1) and low temperature (<100 °C). It is expected to provide useful design and operating guidelines for alleviating thermocline expansion in SHTPB tanks in practical applications.

Table 1 Summary of experimental investigations on SHTPB TES systems.

Studies	Years	Solid fillers	HTFs	T_C/T_H (°C)	ε	H/D_{tank} (m)	Number of thermocouples & arrangement	Diffuser	Insulation	Num./Exp.	Tested parameters in Exp.	Main findings
Faas et al. [32]	1986	Granite Rock and sand	Caloria ® HT 43	179.2/295.5	0.22	12/18.2	--	--	Yes	Exp.	--	• Low Rankine-cycle efficiency of 21% due to limited upper temperature of TES tank.
Meier et al. [33]	1991	Rock	Air	150/550	0.36	1.2/0.15	-- (axial)	--	Yes	Exp.	--	• Considerable heat losses through the wall. • Smaller measured pressure drop than predicted due to low flow resistance near wall.
Pacheco et al. [34]	2002	Quartzite rock & sand	Molten salt	290/390	0.22	6/3	-- (axial and radial)	Yes	Yes	Num./Exp.	--	• Thermocline thickness well predicted by the model. • higher heat loss than predicted due to the lack of insulation on the top cover of the tank.
Yang et al. [35]	2012	Rock	Molten salt	300/500	0.2	2/1	12 (axial)	No	Yes	Num./Exp.	--	• Higher thermal storage capacity and efficiency by using fillers with higher density and specific heat, but also higher entropy generation (Num.).
Yin et al. [22,23]	2014/2017	Zirconium & silicon carbide	Molten salt	290/390	--	0.6/0.12	6 (axial)	Yes	Yes (heating strap)	Exp.	• Inlet HTF temperature • Flow rate • Mixed fillers	• Heat storage efficiency is smaller than 80% due to the thermocline expansion. • Thermocline evolution influenced by HTF velocity. • Piston flow pattern achieved by buffering effect of porous fillers.
Anderson et al. [36]	2014	Alumina	Air	20/120	0.4	10/9.56	-- (5 for axial outer tank surface)	No	Yes	Num./Exp.	--	• Vessel heat loss is acceptable due to only loss 12% of supplied energy.
Bruch et al. [21]	2014	Silica gravel & silica sand	Oil	$\leqslant$ 300	0.27	3/1	250 (for fillers and HTF, axial and radial circle)	Yes	Yes	Num./Exp.	• Cycling number	• No significant inhomogeneity of radial temperature distribution. • Differed thermocline behavior between multiple cycle and single cycle operation. • Impact of metal tank wall on the thermocline moving in charging.
Cascetta et al. [18,29]	2015/2016	Alumina	Air	25/300	0.385 - 0.395	1.8/0.58	19 (axial equally spaced), 5 (radial, decreasing distance), 10 (axial outer surface) 5 (circumferential outer surface)	Yes	Yes	Num./Exp.	• Cycling number	• 40% radial temperature profile affected by metal wall heat, which cannot be predicted by 1D model. • 60% reduction of stored energy after 4 cycles.
Hoffmann et al. [15,30]	2016/2017	Quartzite rock	Rapeseed oil	160/210	0.4	1.8/0.4	32 (axial and radial equally spaced)	No	Yes	Num./Exp.	• Flow rate • Particle size	• Higher heat losses and heat diffusion due to low HTF flow rate. • Stronger forced convection due to high HTF flow rate. • Maximum discharging efficiency of 75% at an optimal flow rate of 0.3 kg s^{-1}.
Al-Azawii et al. [37,38]	2018/2019	Alumina	Air	21.5/150	0.375	1/0.1247	--	Yes (10 cm distance)	Yes	Num./Exp.	• Flow rate	• Higher heat losses due to low HTF flow rate. • Increased exergy efficiency from 35.7% to 55.4% with increasing flow rate from 0.002 to 0.006 m^3 s^{-1}.

Tuttle et al. [39]	2020	Limestone and stone	Air	25/587	0.3	0.9/0.3	8 (axial equally spaced)	--	Yes	Num./Exp.	--	• Relative error on the temperature between particle surface and center larger than 55% at particle Bi_s= 3 (Num.).
Kocak and Paksoy [2]	2020	Demolition wastes	Therminol 66	120/180	0.39	0.9/0.3	9 (axial and radial)	No	Yes	Num./Exp.	• Inlet HTF temperature • Flow rate	• Reduced energy efficiency with the increasing charging temperature. • Thermocline expansion at higher flow rate due to the stratification disturbance. • Thermocline expansion at lower flow rate due to heat loss.
Keilany et al. [40]	2020	Alumina/ Cofalit® rock	Jarysol® oil	100/300	0.417	2.64/1.2	22 (axial and radial)	Yes	Yes	Num./Exp.	• Solid filler	• Good thermal performance of Cofalit® filler than alumina.
Vannerem et al. [26]	2021	Alumina	Jarysol® oil	100/300	0.485	2.64/1.2	22 (axial and radial)	Yes	Yes	Num./Exp.	• Flow rate	• Maximized storage utilization rate (80.6%) at an optimal velocity (Num.). • Robust performance of storage tank under the experimental testing range (100 - 130 °C) and (0.2 - 0.9 kg s^{-1})
Vannerem et al. [41]	2022	Alumina	Jarysol® oil	100/300	0.485	2.64/1.2	63 (axial and radial)	Yes	Yes	Exp.	• Flow distributor	• Solid filler acts as a natural distributor. • Distributor does not influence storage behavior. • Radial homogeneity is then improved at low fluid velocity.
Gautam and Saini [42]	2021	--	Air	<100	--	1.25/0.6	50 (for fillers and HTF, axial and radial)	No (but plenum achieve uniform flow)	Yes	Exp.	• Flow rate • Sizes for particles with pore	• Correlations proposed to predict the Nusselt number.
Bruch et al. [43]	2021	Rock	Water	20/70	--	4/2	5 (axial equal and radial circle)	Yes	No	Exp.	• Flow rate • Inlet HTF temperature	• Cold energy storage system is able to successful store cold at night and compensate performance loss of cooler in daytime.
Alonso and Rojas [44]	2022	Silica/ Soft stone	Air	25/700	0.31/0.37	0.72/0.5	28 (axial and radial, for HTF and outer surface)	--	Yes	Num./Exp.	• Solid filler	• Important role of heat capacity of solid fillers. • Very low heat loss owing to the well-insulated tank walls.
Xu et al. [45]	2022	Aluminum silicate	Water	<60	--	3/1	164 (axial and radial, for HTF and outer surface)	Yes	Yes	Num./Exp.	• Flow rate	• Thermocline stability disturbed by the radial plate-type diffuser. • Model developed based on thermal diffusion to predict the thermocline evolution in axial direction, with an average error of about 13.9%.
Lai et al. [46]	2022	Sintered ore	Air	60/250		0.85/0.32	>7(axial and radial)	No	Yes	Num./Exp.	• Particle size • Flow rate • Diffuser • Insulation	• Air flow increases, the cycle efficiency increases. • Permeability decreases, superficial velocity increases.
This study	2023	Glass sphere	Water	20/70	0.38/0.39	0.4/0.2	32 (axial and radial, for HTF and solid fillers)	Yes	Yes	Num./Exp.	• Particle size • Flow rate • Inlet temperature	--

2. Experimental setup

2.1. Test-rig description

The laboratory-scale SHTPB tank tested has a cylindrical shape with a height of 398 mm and an inner diameter of 194 mm (**Fig. 1a**), the total useful volume being 11.8 L. It has a transparent polycarbonate wall (3 mm thickness) enclosed by an insulation layer made of black nitrile rubber (25 mm thickness). Glass sphere as the sensible filler is packed inside the tank randomly. Water is used as the HTF. The top and bottom ports are simple tubes (Φ= 11.6 mm) located at the center of each cover of the tank. In charging, hot water first enters from the tank top port and transfers heat to solid fillers inside to store heat. In discharging, cold water enters from tank bottom port to drive the stored hot water from tank top to release heat. The charging or discharging stops when each outlet temperature reaches the corresponding threshold point according to the designed requirement.

In total, 32 thermocouples have been used to measure the local temperature at different locations in the storage tank, including 17 for the fluid and 15 for the solid. They were all attached to a plastic tree which has been installed inside the tank carefully (in **Fig. 1b**). In axial direction, both fluid and solid temperatures were measured at 7 heights of the centerline (C in **Fig. 1b**). They are at 49 mm distance one from another and notated as TC-1 to TC-7 from the bottom to the top of the tank. To investigate the radial temperature distribution, the fluid and solid temperatures at the middle (B in **Fig. 1b**; tank diameter coordinate r^*= 0.55) and outer (A in **Fig. 1b**; r^*= 0.95) positions were measured in four radial arms (TC-1; 3; 5; 7). In addition, the inlet and outlet fluid temperatures were also measured at the top and bottom ports, respectively. Thermocouples for glass spheres were installed in the center of sphere and sealed by glue with a similar thermal conductivity as glass (cf. **Fig. 1a**). The fluid thermocouples have been specially attended to avoid contact with the surface of the solid. The influence of contact is negligible with a condition of $1.3>Bi_s>0.1$ due to the conduction resistance of the solid being larger than the convection resistance. The glass was chosen as filler in the experiment, mainly because it has adapted thermal conductivity for operating at a larger Bi_s number and is easily available in diverse sizes on the market.

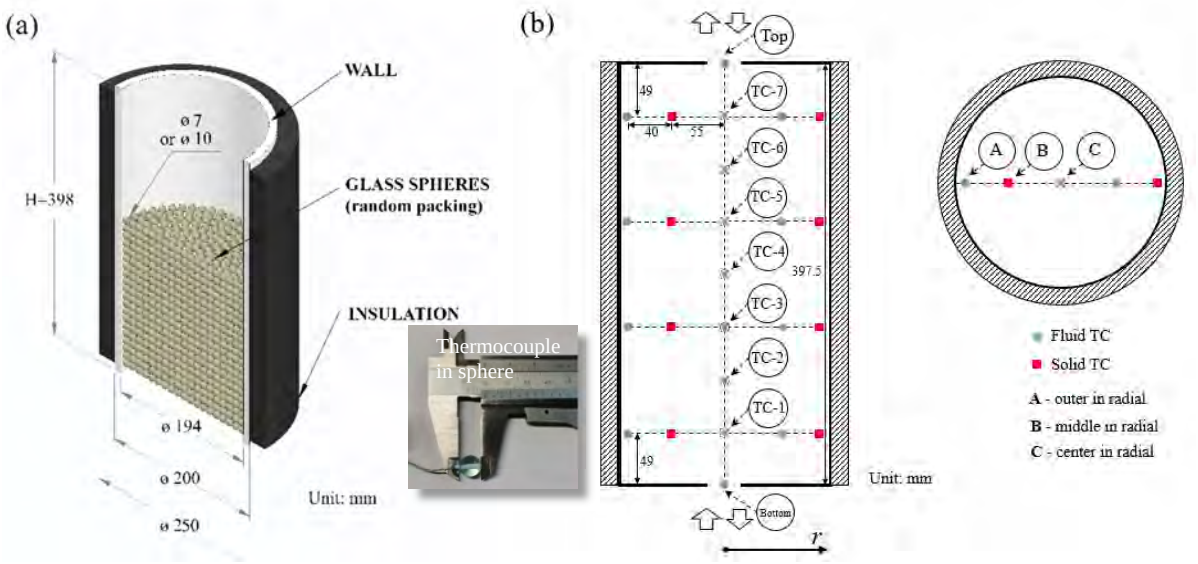

Fig. 1. Laboratory-scale SHTPB tested in LTEN: (a) geometry and dimensions; (b) axial and radial thermocouples locations inside the tank.

Fig. 2 shows the schematic and the photo view of the experimental setup used to study the SHTPB TES system. A hot and cold water tank was used as the hot and cold source for testing the SHTPB tank in charging or discharging, respectively. A PID-controlled electrical heater was installed inside the hot water tank and a low-temperature thermostat with smart cool system (Lauda, RP 855) was connected to the cold water tank and was used to stabilize the water temperature in each tank. Stirring devices were installed in both water tanks, ensuring the homogenous water temperature inside. Two magnetic coupled external gear pumps (Tuthill D-series, 0.07 to 7.63 L min^{-1}) with filters were used to deliver the HTF from the water tank to the top/bottom port of the storage tank. The flow rate of the HTF was controlled and measured by a flow meter (Kobold DPM-1550, 0.05 to 5 L min^{-1}). A reservoir was used to collect the water flowing out from the SHTPB tank for recycling.

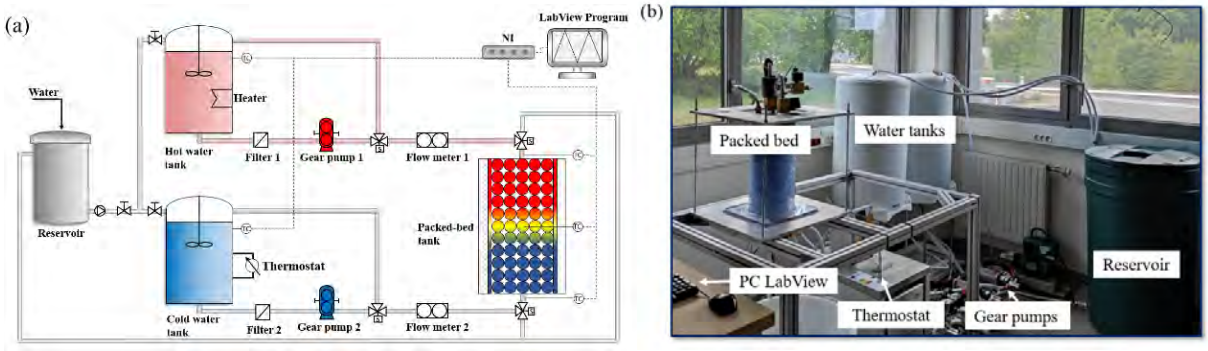

Fig. 2. Schematic view (a) of the experimental test loop and photographic view (b) for the laboratory-scale SHTPB tank (without insulation).

The electronic signals, including the valves, thermocouples, gear pumps, and flow meters, were controlled and recorded by corresponding modules. In particular, the temperature measurements of K-type thermocouples (-75 to 260 °C) were recorded by a temperature input module (NI 9214 and NI 9213) with up to 0.02 °C uncertainty. The recorded signals were monitored at an interval of 0.25 s by using a LabView program developed in-house. The pressure drop was estimated to be very small (ΔP<50 Pa) due to the small tank volume and relatively low flow rate, which could be neglected. A detailed estimation of the measurement uncertainties is presented in Section 4.4.

2.2. Tested cases

Six configurations of SHTPB tank were experimentally investigated to evaluate the impacting factors of inlet configuration and insulation, under different mass flow rates and inlet temperatures, etc., on the thermocline. Detailed parameters of these cases are listed in **Table 2** and introduced as below.

Case 1 vs 3: To verify the temperature gradient inside the particle and to explore the influence of particle size on the thermocline behavior, two sizes of glass spheres of 7 and 10 mm were used as fillers. Case 1 and case 3 were tested under different inlet temperatures and flow rates.

Case 1, 3 vs Case 2, 4: To explore the impact of heat loss on thermocline expansion, two cases (2, 4) without insulation layer were tested and compared to others with insulation (1, 3).

Case 3 vs Case 5, 6: To analyze the buffering effect of porous bed on the allevaiation of inflowing HTF jet, three configurations (Case 3, 5, 6) were tested for comparison, as shown in **Fig. 3**. Case 3 is

the fully packed tank without diffuser, while Cases 5 and 6 introduced the top and bottom diffusers. The plate-type diffuser (6 mm in thickness) having three ring-shaped grooves has been optimized and tested for a single-media thermocline TES tank in our previous works [47]. In Case 5, the space between the diffuser (z_1=10 mm) and the tank top/bottom was filled with one layer of glass spheres to make full use of the tank volume, both the porous bed and the plate diffuser acting as the inlet configuration. In comparative Case 6, no solid fillers were packed in this gap to eliminate the effect of porous fillers, and the height was set to be larger (z_1=35 mm) to amplify the impact of inflowing jet and mitigating effect of the plate-type diffuser. In this way, the effects of the diffuser on the radial temperature distribution, the impacted height, and and the global thermal efficiency were investigated under different inlet temperatures and flow rates.

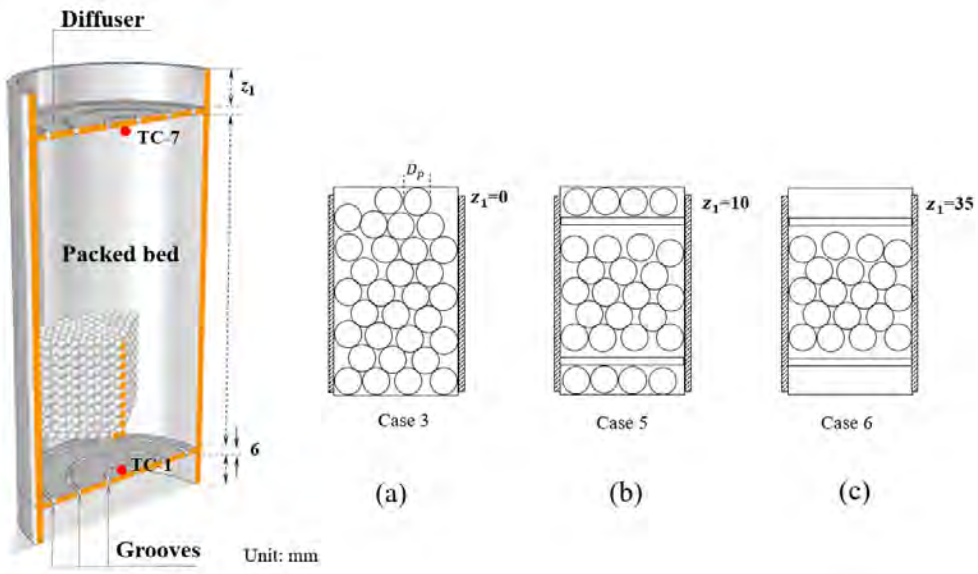

Fig. 3. Different inlet diffuser configurations experimentally tested in this study: (a) only porous bed; (b) porous bed & plate diffuser; (c) only plate-type diffuser.

Table 2 Tested SHTPB configurations with different operational conditions.

Configuration	Geometry parameters				Operational parameters	
	Particle diameter (mm)	Porosity (-)	Diffuser position (mm)	Insulation thickness (mm)	Flow rates (L min^{-1})	Inlet temperature (°C)
	D_p	ε	z_1	--	$\dot{V}_f$	T_C/T_H
Case 1	7	0.38	--	25	0.3/0.5/1.0/1.5	20/(50, 60, 70)
Case 2	7	0.38	--	--	0.3	20/70
Case 3	10	0.39	--	25	0.3/0.5/1.0/1.5	20/(50, 60, 70)
Case 4	10	0.39	--	--	0.3	20/70
Case 5	10	0.39	10	25	0.3/0.5/1.0/1.5	20/(50, 60, 70)
Case 6	10	1 (non-bed region) + 0.39 (bed region)	35	25	0.3/0.5/1.0/1.5	20/(50, 60, 70)
Case 1 vs Case 3: effect of particle size on the temperature gradient inside the sphere.						
Case 1, 3 vs Case 2, 4: effect of insulation on the thermocline dynamics and system's efficiency.						
Case 3 vs Case 5, 6: effect of diffuser on the thermocline dynamics and system's efficiency.						

3. Numerical model

A dispersion-concentric three-phase (DC-3P) numerical model has been developed based on the following assumptions:

(1) HTF is incompressible plug flow.

(2) Thermophysical properties of fluid and solid are set as constant (**Table 3**).

(3) Solid sphere is modeled as dispersion concentric because of the possible non-ignorable temperature gradient inside (Bi_s>0.1).

(4) Wall is modeled as a separate phase in 1D (axial direction), taking the wall impact (heat storage/release in the wall) into account [31].

(5) Insulation layer is simplified and represented by a thermal resistance based on our earlier study [31].

(6) Heat loss to the environment considers both the natural convection and the radiation.

With these assumptions, the governing equations for computation domain (**Fig. 4**) can be written as follows.

Table 3 Thermophysical properties of different materials used in this study.

	Material	Density (kg m^{-3})	Heat capacity (J kg^{-1} K^{-1})	Thermal conductivity (W m^{-1} K^{-1})	Dynamic viscosity (Pa s)
	--	ρ	C_p	λ	μ
Fluid (47.5 °C) [48]	Water	990	4187	0.634	5.8×10^{-4}
Ambient (20 °C, 100 kPa)	Air	1.17	1004	2.63×10^{-2}	1.8×10^{-5}
Solid media (20 °C)	Soda lime glass	2463	840	1.129	--
Wall (20 °C)	Transparent polycarbonate	1200	1170	0.200	--
Insulation (20 °C)	Black nitrile rubber	160	1350	0.0412	--

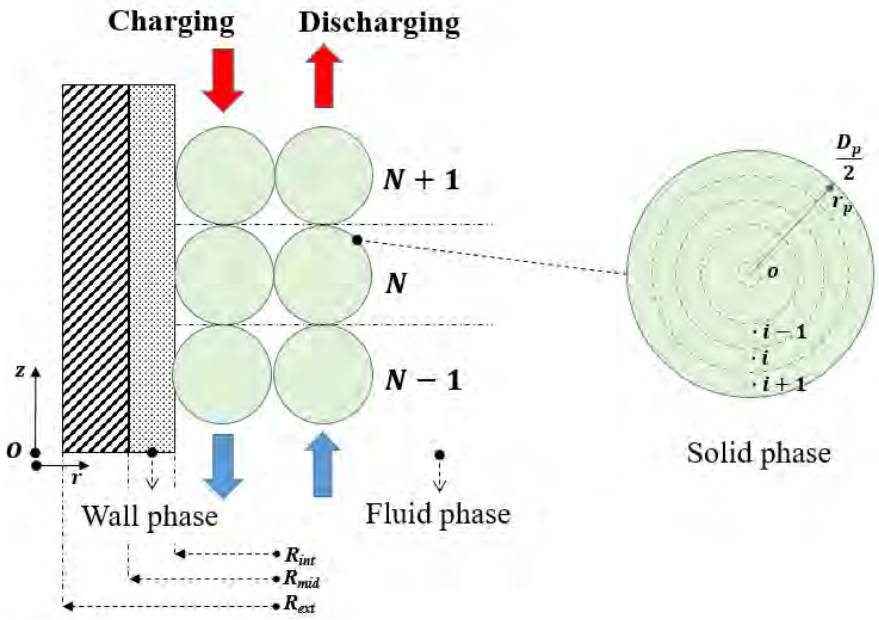

Fig. 4. Schematic of numerical resolution domain for the developed DC-3P model.

3.1. Governing equations

Fluid [49]:

$$\varepsilon \cdot \rho_f \cdot C_{p,f} \cdot \left[\frac{\partial T_f(z)}{\partial t} + u_f \cdot \frac{\partial T_f(z)}{\partial z}\right] = \frac{\partial}{\partial z} \cdot \left[\lambda_{f,eff} \cdot \frac{\partial T_f(z)}{\partial z}\right] + h_{sf} \cdot \frac{A_s}{V_s} \cdot \left[T_s'\left(z, r_p = \frac{D_p}{2}\right) - T_f(z)\right] + h_{f-w} \cdot \frac{A_{f-w}}{V_b} \cdot [T_w(z) - T_f(z)] \quad (1a)$$

Solid filler (2D spherical radius coordinate):

$$\rho_s \cdot C_{p,s} \cdot \frac{\partial T_s(z,r_p)}{\partial t} = \frac{1}{r_p^2} \cdot \frac{\partial}{\partial r_p} \cdot \left[r_p^2 \cdot \lambda_s \cdot \frac{\partial T_s(z,r_p)}{\partial r_p}\right] \quad (1b)$$

Wall:

$$\rho_w \cdot C_{p,w} \cdot \frac{\partial T_w(z)}{\partial t} = \frac{\partial}{\partial z} \cdot \left[\lambda_w \cdot \frac{\partial T_w(z)}{\partial z}\right] + h_{f-w} \cdot \frac{A_{f-w}}{V_w} \cdot [T_f(z) - T_w(z)] + h_{w-amb} \cdot \frac{A_{f-w}}{V_w} \cdot [T_{amb} - T_w(z)] \quad (1c)$$

where T temperature, t time, u interstitial velocity, ε porosity, C_p specific heat, ρ density, λ thermal conductivity, h heat transfer coefficient (HTC), A superficial area, and V volume are presented; z is the axial and r_p is the spherical coordinate; subscript of *f*, *s*, *w*, *eff*, *amb* represent fluid, solid, wall, effective value, and ambient, respectively; For example, T_s' is the solid surface temperature, T_w is the wall temperature calculated at wall middle position of $\frac{(R_{int}+R_{mid})}{2}$, and the ratios of area to volume are defined as:

$$\frac{A_s}{V_s}=\frac{6\cdot(1-\varepsilon)}{D_p},\quad \frac{A_{f-w}}{V_b}=\frac{R_{int}+R_{mid}}{R_{int}^2},\quad \frac{A_{f-w}}{V_w}=\frac{R_{int}+R_{mid}}{R_{mid}^2-R_{int}^2} \tag{2}$$

where R_{int} and R_{mid} are internal and middle radius of tank, and D_p is the particle diameter (cf. **Fig. 4**).

The effective fluid thermal conductivity ($\lambda_{f,eff}$) in axial direction contributed by stagnant thermal diffusion and turbulent thermal contribution is given as:

$$\lambda_{f,eff}=\varepsilon\cdot\lambda_f+0.5\cdot Re\cdot Pr\cdot\lambda_f \qquad (Re>0.8) \tag{3}$$

The convection term between solid filler surface and HTF is added in the boundary condition which will be introduced in later text. The solid-fluid HTC (h_{sf}) is calculated as:

$$h_{sf}=\left(\frac{\lambda_f}{D_p}\right)\cdot\left\{1.26\cdot\left[\frac{1-(1-\varepsilon)^{\frac{5}{3}}}{2-3\cdot(1-\varepsilon)^{\frac{1}{3}}+3\cdot(1-\varepsilon)^{\frac{5}{3}}-2\cdot(1-\varepsilon)^2}\cdot Re\cdot Pr\right]^{\frac{1}{3}}\right\} \qquad (Re<74) \tag{4a}$$

The equivalent HTC of fluid-to-wall center (h_{f-w}) and the equivalent HTC of wall center-to-ambient (h_{w-amb}) are defined as:

$$\frac{1}{h_{f-w}}=\frac{1}{h_{int}}+\frac{1}{\lambda_w}\cdot\ln\left(\frac{R_{int}+R_{mid}}{2\cdot R_{int}}\right)\cdot R_{int} \tag{4b}$$

$$\frac{1}{h_{w-amb}}=\left[\frac{1}{\lambda_w}\cdot\ln\left(\frac{2\cdot R_{mid}}{R_{int}+R_{mid}}\right)+\frac{1}{\lambda_{ins}}\cdot\ln\left(\frac{R_{ext}}{R_{mid}}\right)+\frac{1}{h_{ext}+h_{rad}}\cdot\frac{1}{R_{ext}}\right]\cdot R_{int} \tag{4c}$$

where the fluid-to-wall convective HTC (h_{int}) on inner wall surface (**Eq. 5a**), the insulation-to-ambient air convective HTC (h_{ext}) on outer insulation surface based on a correlation of natural convection on vertical standing wall (**Eq. 5b**), and radiative HTC (h_{rad}) based on the Stefan–Boltzmann law (**Eq. 5c**), are all regarded as constant and calculated based on the tank outer surface temperature when the fluid temperature is equal to ($T_{ave}=\frac{T_C+T_H}{2}$):

$$h_{int}=\left(\frac{\lambda_f}{H}\right)\cdot 0.6\cdot Re^{\frac{1}{2}}\cdot Pr^{\frac{1}{3}},\qquad (1<Re<40) \tag{5a}$$

$$h_{ext}=\left(\frac{\lambda_{air}}{H}\right)\left\{0.825+\frac{0.387\cdot Ra_{air}^{\frac{1}{6}}}{\left[1+\left(\frac{0.492}{Pr_{air}}\right)^{\frac{9}{16}}\right]^{\frac{8}{27}}}\right\}^2 \qquad (Ra_{air}<10^{12}) \tag{5b}$$

$$h_{rad} = \frac{\epsilon \cdot \sigma \cdot (T^4 - T_{amb}^4)}{T - T_{amb}} \quad (5c)$$

where all empirical correlations used have been introduced in our previous work [39] and all dimensionless numbers (Re, Ra, Pr) are defined and listed in the ***nomenclature***.

3.2. Boundary and initial conditions

In a charging/discharging process, the boundary and initial condition are described in **Table 4**. It assumes that the initial condition of charging is fully discharged and with a homogenous coldest operating temperature, while the cutoff temperature after charging is the beginning of discharging. The model was solved with the MATLAB function ode45 for the time derivatives after the convergence study, as introduced in Supplementary Material S1 (in Fig. S1). **Fig. 5** illustrates a flow chart of numerical algorithm of the DC-3P model and calculation of system's efficiency.

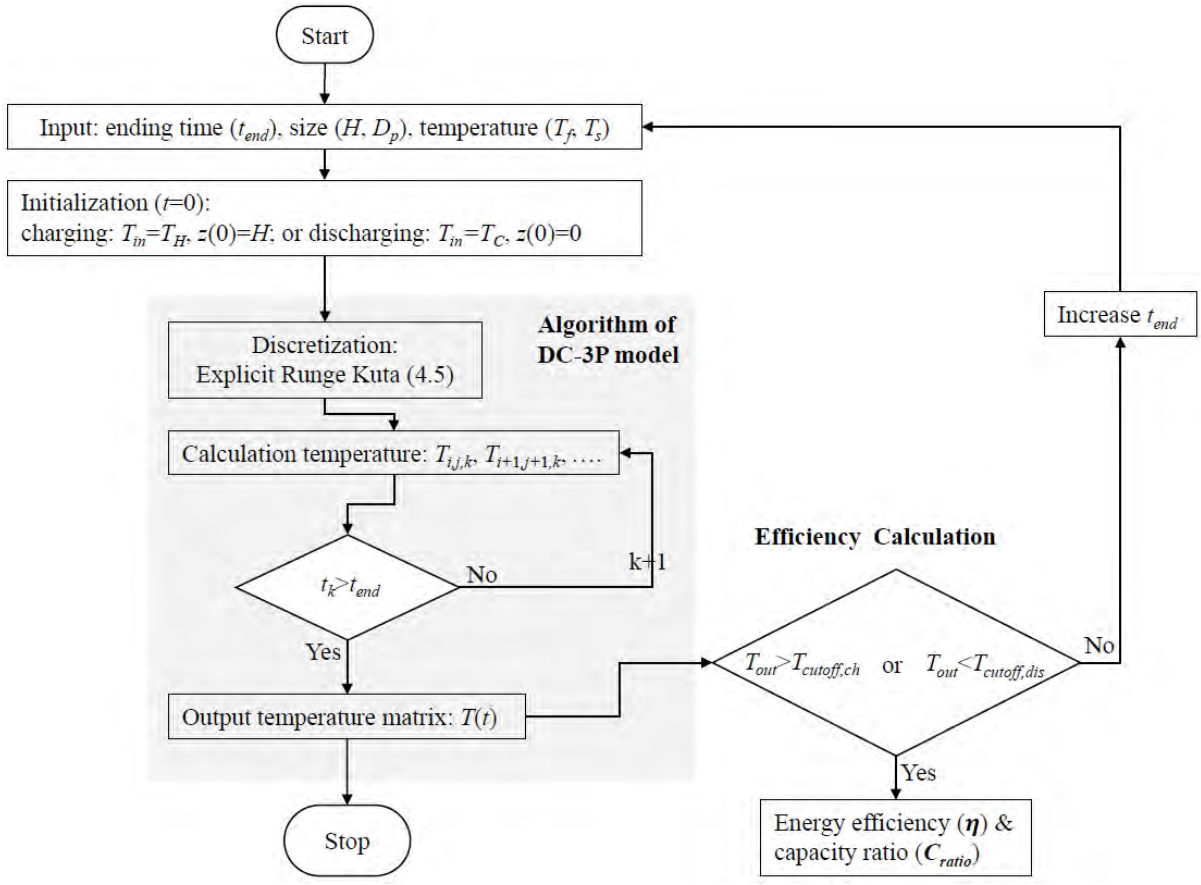

Fig. 5. Flow chart: numerical algorithm of the DC-3P model and calculation of system's efficiency.

Table 4 Initial and boundary condition in axial z-direction and spherical radius r_p-direction.

Initial condition (t=0)			
All domains	$T_s = T_f = T_w = T_{ini}$, where $T_{ini} = T_C$, (Ch) $T_{ini} = T_{cutoff,ch}$, (Dis)	$z \in [0, H]$	$r_p \in \left[0, \frac{D_p}{2}\right]$
Boundary condition ($t \geq 0$)			
Surface of solid particle	$-\lambda_s \cdot \frac{\partial T_s(z,t)}{\partial r_p} = h_{sf} \cdot (T_s' - T_f)$	$z \in [0, H]$	$r_p = \frac{D_p}{2}$
Center of solid particle	$\frac{\partial T_s(z,t)}{\partial r_p} = 0$	$z \in [0, H]$	$r_p = 0$
Tank top & bottom	$\frac{\partial T_s(z,t)}{\partial z} = \frac{\partial T_w(z,t)}{\partial z} = 0$	$z = 0, \& \, z = H$	$r_p \in \left[0, \frac{D_p}{2}\right]$
Inlet HTF	$T_f(z = H, t) = T_H$, (Ch) $T_f(z = 0, t) = T_C$, (Dis)	--	--
Outlet HTF	$\frac{\partial T_f(z=0,t)}{\partial z} = 0$, (Ch) $\frac{\partial T_f(z=H,t)}{\partial z} = 0$, (Dis)	--	--

4. Key performance indicators and associated uncertainty

Several indicators are used to assess the thermocline expansion as well as the overall performance of the SHTPB tank, introduced as follows.

4.1. Charging/discharging time

The charging/discharging cutoff time (t_{cutoff}) relies on the threshold or cutoff outlet fluid temperature at the termination condition, defined as **Eq. 6** in this study [50].

$$T_{cutoff,ch} = T_H - 20\% \cdot (T_H - T_C) \tag{6a}$$

$$T_{cutoff,dis} = T_C + 20\% \cdot (T_H - T_C) \tag{6b}$$

where the outlet temperature threshold coefficient (θ) is equal to 0.2 which is considered useful in generation of superheated steam in CSP plant, usually used in many works [30][51–53]. It means the outlet fluid temperature changes by 20% of the operational temperature difference in charging and discharging. Nevertheless, the coefficient of θ is determined arbitrarily, discussing between 0.05, 0.1,

and 0.3 etc., and its selection is only used to compare performance in different tanks. Therefore, it's necessary to choose the value depending on the experimental requirements or the application of interest.

Normalized parameters are defined for a better comparison under different operational conditions. Two types of dimensionless time for different conditions were used: one is the dimensionless time based on flow rate, t^*, as a ratio of actual time to the residence time of HTF flowing through the tank in a plug flow pattern. Another is the dimensionless time based on the energy, t_E^*, as the ratio of input energy by HTF to maximum stored energy inside the tank used in Supplementary Material.

$$t^* = t \cdot \frac{u_f}{H} \tag{7a}$$

$$t_E^* = t \cdot \frac{\dot{m}_f \cdot C_p \cdot (T_H - T_C)}{\Delta E_{stored,max}} \tag{7b}$$

z^* and T^* is the dimensionless height and dimensionless temperature, defined as:

$$z^* = \frac{z}{H} \tag{7c}$$

$$T^* = \frac{T - T_C}{T_H - T_C} \tag{7d}$$

4.2. Thermocline thickness

The dimensionless thermocline thickness ($L^*_{thermocline}$) is determined by the length of stratification region in bed [54], according to the physical boundary within a certain temperature range before reaching the top or bottom of the tank.

$$L^*_{thermocline} = \frac{z\{T = T_C + n\% \cdot (T_H - T_C)\} - z\{T = T_H - n\% \cdot (T_H - T_C)\}}{H} \tag{8}$$

In charging, $z\{T = T_C + n\% \cdot (T_H - T_C)\} > 0$;

In discharging, $z\{T = T_H - n\% \cdot (T_H - T_C)\} < H$;

where n is a threshold value that is defined as the hottest/coldest temperature differs n % to the operational temperature range $(T_H - T_C)$, setting as 5% in this study. In experiment, the thermocline thickness is calculated based on the fluid temperature variation at the axial centerline of the storage tank.

4.3. Energy efficiency and capacity ratio

The charging process is discussed in this study. The stored energy (ΔE_{stored}) is the amount of thermal energy stored in solid and fluid phases from beginning (t=0) to ending (t=t_{ch}) in charging. Charging energy efficiency (η_{ch}) is thus defined as the ratio of the stored energy of ΔE_{stored} to the input energy by HTF (ΔE_{in}).

$$\eta_{ch} = \frac{\Delta E_{stored}}{\Delta E_{in}} = \frac{\Delta E_{stored}(t=t_{ch}) - \Delta E_{stored}(t=0)}{\int_0^{t_{ch}} [\dot{m}_f \cdot C_{p,f} \cdot (T_{in} - T_0)] dt} \quad (9a)$$

where T_{in} is the inlet temperature of HTF and T_o is the reference temperature (20 °C), respectively.

The heat loss ratio of charging ($\eta_{ch,loss}$) is defined as the ratio of the heat loss (ΔE_{loss}) to the total input energy (ΔE_{in}) in charging.

$$\eta_{ch,loss} = \frac{\Delta E_{loss}}{\Delta E_{in}} = \frac{\int_0^{t_{ch}} [\dot{m}_f \cdot C_{p,f} \cdot (T_{in} - T_{out})] dt - \Delta E_{stored}}{\int_0^{t_{ch}} [\dot{m}_f \cdot C_{p,f} \cdot (T_{in} - T_0)] dt} \quad (9b)$$

where T_{out} is the outlet temperature of the HTF.

Capacity ratio (C_{ratio}) [55,56] in charging is the ratio of the actual stored energy to the theoretical maximum stored energy.

$$C_{ratio} = \frac{\Delta E_{stored}}{\Delta E_{stored,max}} = \frac{\Delta E_{stored,s} + \Delta E_{stored,f}}{\Delta E_{stored,max,s} + \Delta E_{stored,max,f}} \quad (9c)$$

In addition, the stored energy in the tank at a certain time for fluid and solid is calculated in modeling:

$$\Delta E_{stored}(t) = \pi \cdot R_{int}^2 \cdot \int_0^H \left[\rho_f \cdot C_{p,f} \cdot \varepsilon \cdot (T_f - T_0) + \rho_s \cdot C_{p,s} \cdot (1-\varepsilon) \cdot (\bar{T}_s - T_0)\right] dz \quad (9d)$$

where $\bar{T}_s$ is the average temperature of single solid spheres at the same height. In experiment, the stored energy is calculated using the average temperatures of solid and fluid for a number of small unit volumes. More precisely, the tank volume is firstly divided into small cells by thermocouple points and the temperature of such single unit volume is considered as homogenous.

4.4. Uncertainty analysis

The uncertainties of experimentally measured parameters and calculated parameters are listed in **Table *5***. Based on the calibrating measurement results in Supplementary Material S2, details of uncertainty analysis are discussed in S3.

Table 5 The uncertainties of measured and calculated parameters.

Measured parameters		Uncertainties
Temperature	T	± 0.37 K
Volumetric flow rate	$\dot{V}_f$	± 1%
Particle diameter*[1]	D_p	± 0.1 mm
Solid density*[1]	ρ	± 1.6% (40 kg m^{-3})
Thermal conductivity*[1]	λ	± 0.001 W m^{-1} K^{-1}
Specific heat capacity*[1]	C_p	± 8 J kg^{-1} K^{-1}
Calculated parameters*[2]		
Porosity	ε	± 0.004
Energy efficiency	η_{ch}	± 5%
Capacity ratio	C_{ratio}	± 2%
Thermocline thickness	$L^*_{thermocline}$	± 5% (20 mm)

Assess measurement error:

***1** The standard uncertainty is defined by standard deviation: $SD = \sqrt{\frac{1}{n}\sum_{i=1}^{n}(x_i - \bar{x})^2}$, where x is measured parameter and n is the repeated measurement times [57].

Assess calculation error:

***2** The components uncertainty is defined as $:\vartheta = \sqrt{\sum_{j=1}^{m-1}\left(\frac{\partial y}{\partial x_j} SD_{x_j}\right)^2}$, where $y = f(x_1, x_2 \ldots . . x_m)$ is the in-directly parameter, and m is the number of components [58].

5. Results and discussion

This work experimentally investigated the thermocline expansion of SHTPB TES system due to various factors, including the inlet diffuser configuration, the insulation, the filler diameter, the HTF flow rate and the working temperatures. The developed DC-3P was firstly validated by comparison with the experimental data and then was used to conduct numerical parametric study.

5.1. Comparison between numerical and experimental results

Validation and comparison between numerical (DC-3P) and experimental results are performed to address some interesting but inadequately investigated issues, including the temperature distribution of tank, the temperature gradient inside the solid particles, and the applicable range of the DC-3P model.

5.1.1. Fluid temperature profiles validation

The experimental data of Case 1 (D_p=7 mm, Péclet number Pe=12, Particle Reynolds number Re=3, Bi_s=0.76, charging process) was first used for numerical model validation. **Fig. 6a** shows the comparison of fluid temperature evolution at axial positions (cf. C in **Fig. 3b**; r=0). At first sight, a good agreement between numerical and experimental results can be found. **Fig. 6b** further shows the variation of temperature difference (ΔT) vs. charging time. The corresponding standard deviation (SD) is calculated based on **Eq. 10**. For most of the thermocouples in the axial centerline of the tank, ΔT< ±2.5 °C and SD< 0.7 °C can be observed, indicating that the temperature evolution at these positions can be well predicted by the developed DC-3P model. However, for TC-7 near the top inlet, the discrepancy ($\Delta T \approx$10 °C and $SD \approx$2 °C) is still noticeable, implying the possible departure from the assumed plug flow used in this 1D model at this position. This is mainly due to the impact of inflowing HTF jet on the radial velocity distribution and consequently on the thermocline expansion and evolution, which will be further investigated in detail and discussed in later sub-sections.

During charging process, the energy efficiency difference at the cutoff time between numerical and experimental results is around 2%, which is within the experimental uncertainty of 5% (cf. **Fig. S4**). At a final cutoff fluid outlet temperature of 43.8 ° C (θ=0.2), the energy efficiency is calculated to be η_{ch}=83.3% by modelling and is η_{ch}=85.5% in experiment, showing a good agreement. In conclusion, the DC-3P model has a good accuracy in simulating the large-size sphere (Bi_s>0.1) and tank with a large wall volume of SHTPB.

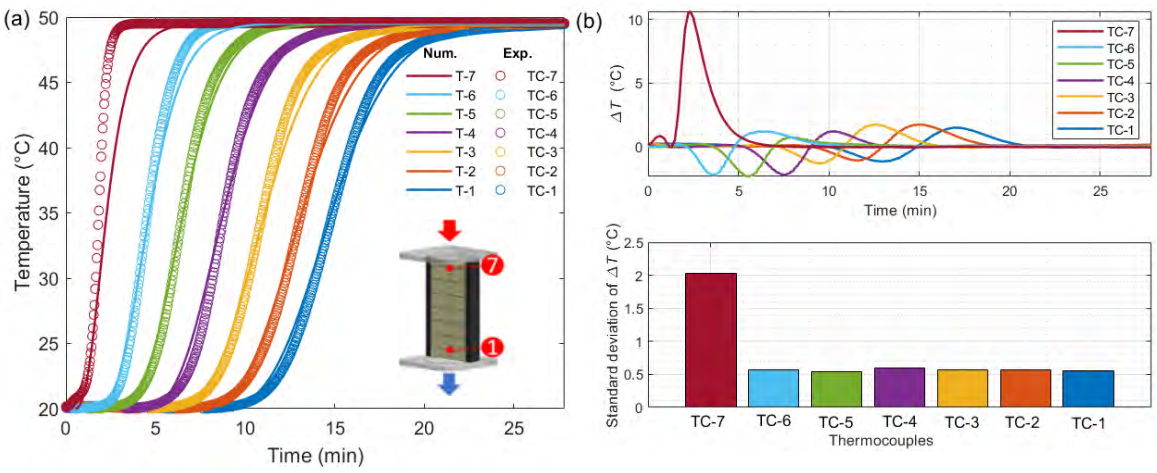

Fig. 6. Comparison between numerical results and experimental data: (a) Evolution of fluid temperature at different locations of axial centerline; (b) fluid temperature differences and corresponding standard deviations (Case 1: T_C/T_H=20/50 °C, D_p=7 mm, $\dot{V}_f$ =0.5 L min^{-1}, Pe=12, Re=3, Bi_s=0.76, charging operation).

$$SD = \sqrt{\frac{1}{N}\sum_{i=1}^{N}[\Delta T(t) - \overline{\Delta T}(t)]^2} \tag{10a}$$

$$\Delta T(t) = T_{exp.}(r = 0, z, t) - T_{num.}(r = 0, z, t) \tag{10b}$$

5.1.2. Temperature gradient inside sphere particles

The temperature gradient inside sensible fillers, reflected by the temperature difference between the solid sphere center and the surrounding HTF, has been reported by numerical modelling but inadequately investigated nor validated in experiments. To address this question, **Fig. 7** presents the time and volume-averaged temperature gap between solid sphere center and fluid as defined in **Eq. 11**, obtained both by experimental measurements of all thermocouples and by DC-3P modelling. The solid Biot number Bi_s ranges from 0.6-1.1 for 7 mm sphere fillers (Case 1) and from 0.7-1.2 for 10 mm sphere fillers (Case 3) under the tested flow rates, implying that the dispersion-concentric model is necessary to be used [59]. Both numerical and experimental results show that the $\Delta\bar{T}_{sf}$ increases with the increasing of flow rate and inlet fluid temperature (T_H). Comparing two sphere sizes, the difference between the numerical and experimental results is smaller than 0.3 °C for 10 mm fillers and about 1 °C

for 7 mm fillers, respectively, showing good agreement. Contrary to theory, the temperature gap in experiments is larger for small-size particles, maybe due to heat transfer area difference of the flow thermal front [15] as well as the measurement uncertainties and difficulties. But in general, the $\Delta\bar{T}_{sf}$ value up to 1.7 K can be detected in experiments and due to the large Bi_s number, the conduction resistance of the solid sphere is much higher than the convection resistance between the fluid and solid. Thereby, the temperature difference confirms the existence of noticeable temperature gradient inside sphere under certain circumstances which is verified in experiments for the first time.

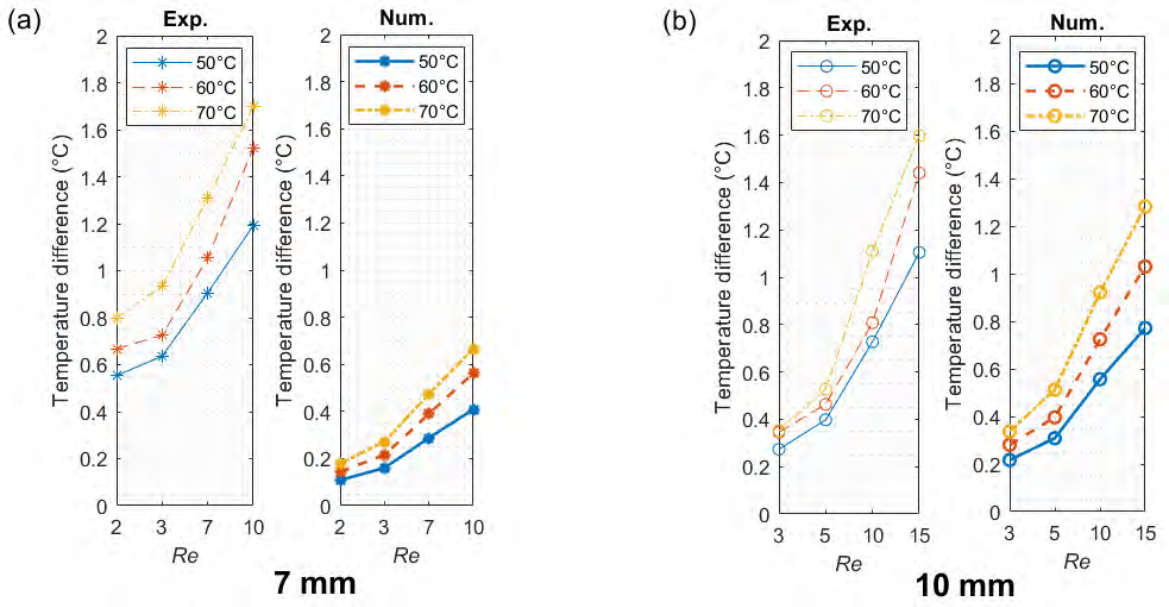

Fig. 7. Average temperature difference between sphere center and fluid in charging process: comparison between experimental and numerical results. (a) D_p=7 mm; (b) D_p=10 mm

$$\Delta\bar{T}_{sf}\ (K) = \frac{\int_0^H \int_0^{t_{cutoff}} [T_f - T_s(r=0)]dtdz}{H \cdot t_{cutoff}} \tag{11}$$

5.1.3. Validity range of the DC-3P model

Numerical and experimental results are compared for the investigated Case 1 and Case 3 in order to determine the precision or applicable range of the developed DC-3P model. **Fig. 8** reports the value of temperature standard deviation (*SD*) and the energy efficiency difference ($\Delta\eta_{ch}$) obtained under various operating conditions. Result show that within the tested condition of Re <15 and Bi_s<1.3, the SD and $\Delta\eta_{ch}$ can be kept below 2.5 K and 3%, respectively. The developed DC-3P model could thereby

be safely used with good precision under this applicable range even though the inlet HTF penetration has a non-negligible effect on the thermocline expansion.

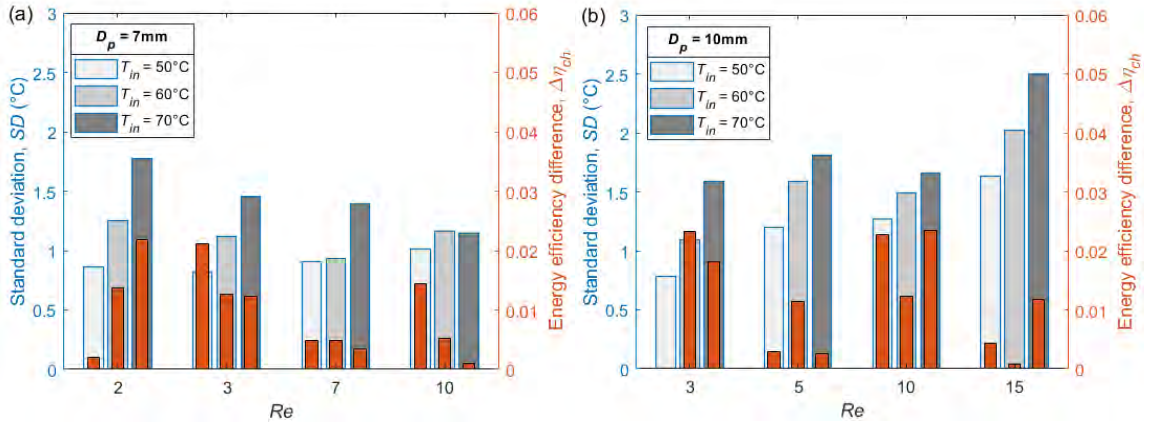

Fig. 8. Comparison of numerical and experimental results on temperature standard deviation (*SD*) and energy efficiency difference ($\Delta\eta_{ch}$) in charging process: (a) Case 1 (D_p=7 mm); (b) Case 3 (D_p=10 mm).

5.2. Experimental study on the influence of inlet configuration and insulation

5.2.1. Evolution of temperature field

Fig. 9 shows the evolution of the fluid temperature cartography inside the SHTPB tank experimentally measured for one fully charging and discharging cycle. Case 3 with porous bed inlet (D_p=10 mm) has been tested at two flow rates, i.e., $\dot{V}_f$=0.3 (Re=5) and 1.5 L min^{-1} (Re=15), to highlight the impact of inflowing jet on the thermocline expansion in SHTPB. The colormap is constructed from data interpolation of 17 thermocouples measurements (linear interpolation in the axial direction). The dimensionless time equaling t^*=1 (cf. **Eq. 7a**) means that the theoretical plug flow reaches the tank top or bottom. It can be observed that at the beginning of charging (t^*=0), the tank has a quasi-homogeneous temperature of T_C (blue color). But for the beginning of discharging, the temperature distribution inside tank is a bit less homogeneous since the ending of fully charging (θ=0.01, for better observation) has been used as the initial condition for discharging.

By examining the temperature color maps, it can be observed that the thermocline region grows thicker over charging or discharging time. Moreover, the shape of thermocline region is not flat,

indicating that temperature gradient exists in the radial direction. The impact of penetrating flow inject on the thermocline expansion can be clearly seen, especially with a high flow rate ($\dot{V}_f$=1.5 L min^{-1}) involving a more important inertial force. It seems that the solid fillers alone are not totally capable of buffering the momentum-dominated injecting flow under this tested condition, resulting in the non-uniform fluid distribution which destabilizes the temperature stratification. Note that the shape of thermocline is a little bit different in charging and discharging due to the influence of the gravity and the lowered temperature at the near-wall region (heat loss).

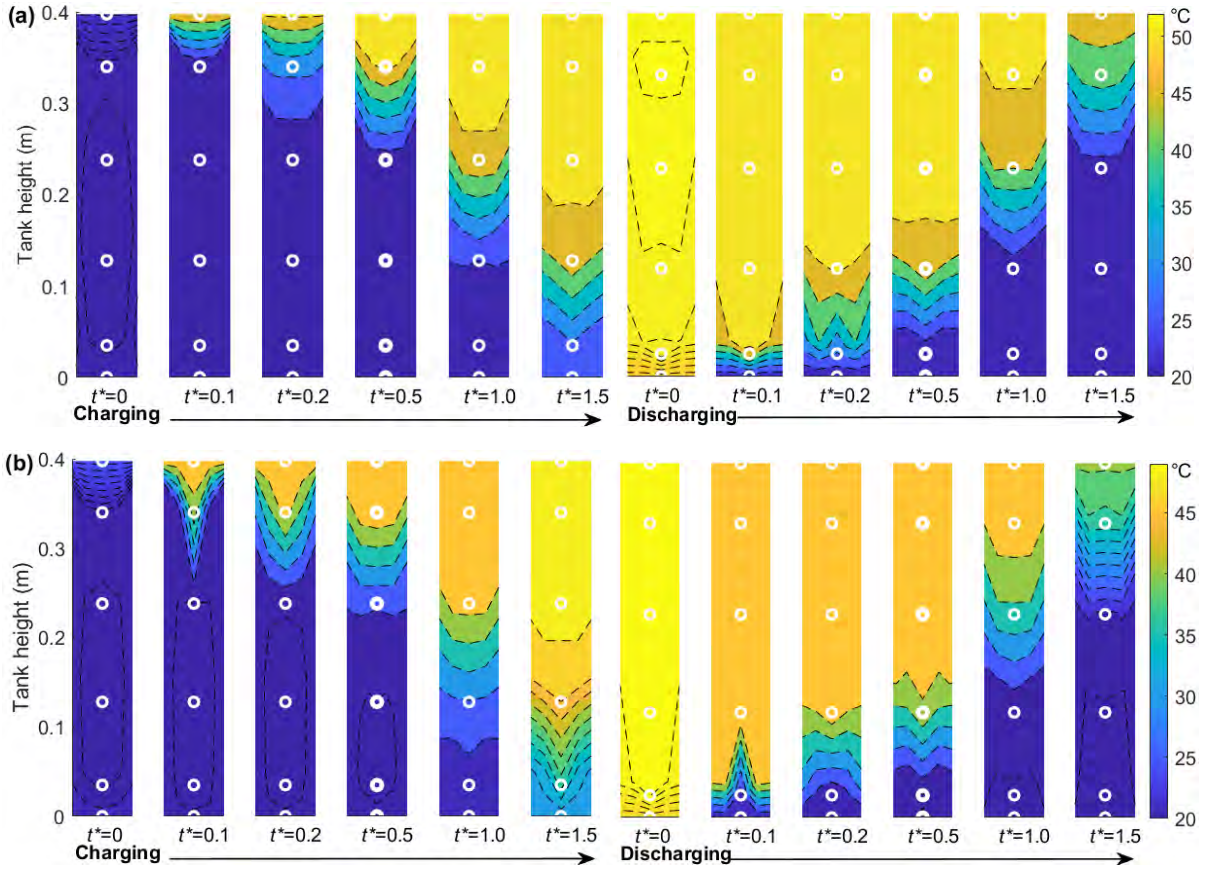

Fig. 9. Evolution of fluid temperature distribution experimentally measured for one charging-discharging cycle (Case 3: T_C/T_H=20/50 °C, D_p=10 mm): (a) $\dot{V}_f$=0.3 L min^{-1}; (b) $\dot{V}_f$=1.5 L min^{-1}.

5.2.2. Impact of inlet configuration

The testing results of Case 3 (packed bed), Case 5 (packed bed + diffuser) and Case 6 (diffuser) in **Fig. 3** are compared to assess the performance of different inlet configurations to mitigate the impact of penetrating flow injection. **Fig. 10** shows the evolution of radial fluid temperature differences over

charging time for the center to outer (T^C-T^A) and for the center to the middle (T^C-T^B) positions at TC-7 (near the top inlet, under the diffuser; z*=0.875) and TC-5 (near middle tank height; z*=0.625) levels. A non-uniformity factor (f_r) defined as the maximum temperature difference in radial direction to the operating temperature range (**Eq. 12**) is introduced to indicate the (non)-uniformity of radial temperature distribution, as presented at the upper-right corner of **Fig. 10**. When the value of f_r approaches 0, there is almost no radial temperature gradient, indicating that the shape of thermocline is flattened as assumed in 1D numerical model. From **Fig. 10a**, it can be seen that the radial temperature difference (ΔT) at TC-7 level decreases after adding the plate-type diffuser. The corresponding value of f_r is 0.83 for basic Case 3 (z_1=0, only the packed bed), 0.66 for Case 6 (z_1=35 mm, only the diffuser), and 0.30 for Case 5 (z_1=10 mm, the combined diffuser and packed bed), respectively. As expected, the combined effect of diffuser and packed bed largely alleviates the influence of penetrating HTF jet on the thermocline stability in the entrance, better than that with only the diffuser or only the packed bed.

At TC-5 level near the middle tank height, the impact of penetrating HTF jet on the radial temperature distribution uniformity is shown to be rather limited even at high flow rate, reflected by the small radial temperature differences and low f_r values (<0.2) for all tested inlet configurations (**Fig. 10b**). The outer radial temperature of Case 6 (no packed bed in the entrance region) is a little higher than the center temperature because of the double-hump shape of thermocline caused by higher velocity in near-wall region [56]. Without packed bed in the entrance, the double-hump phenomenon is more obvious so that the f_r value for Case 6 is higher than other configurations.

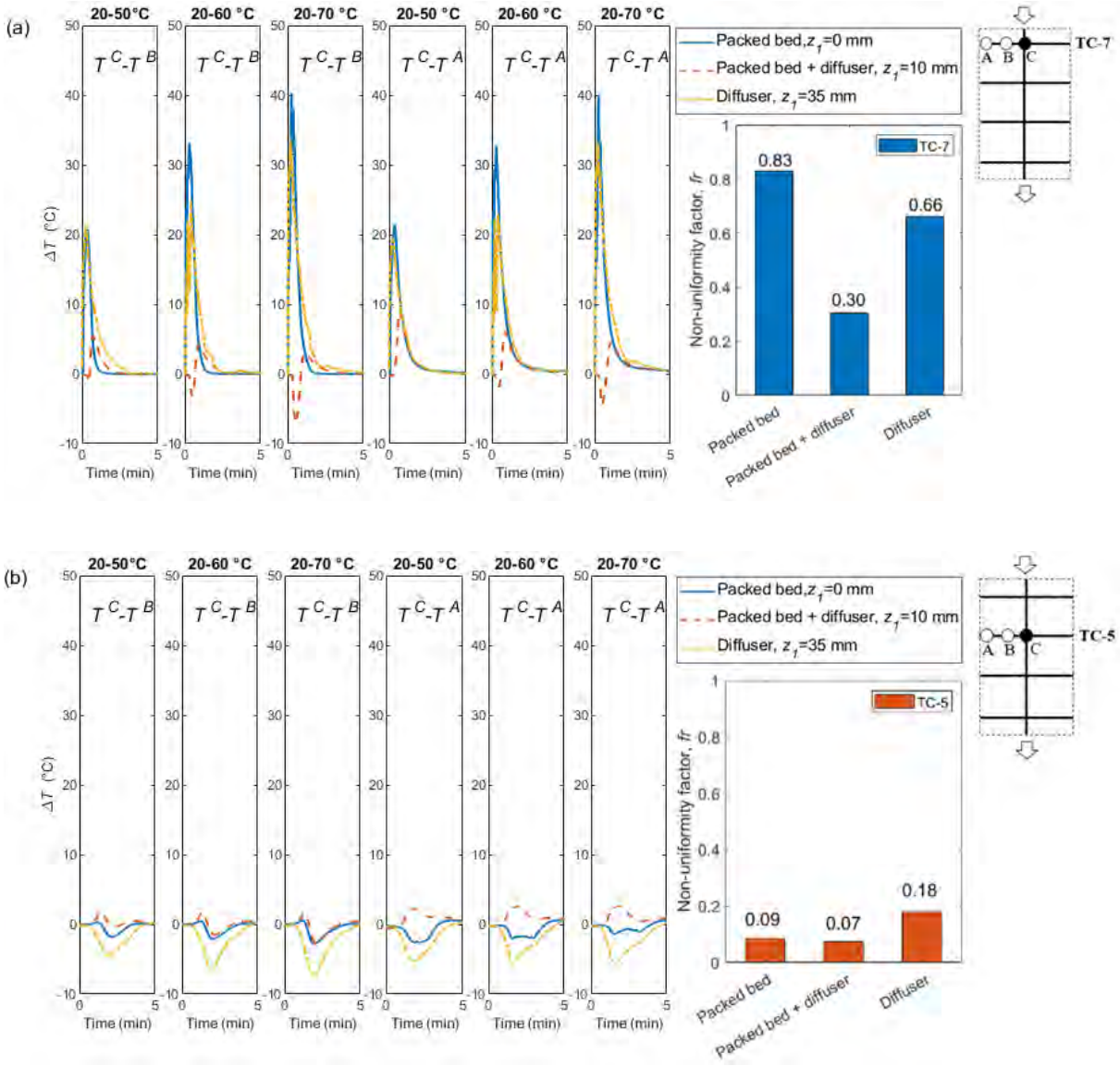

Fig. 10. Radial temperature difference inside the SHTPB tank with different tested inlet configurations: (a) TC-7 position; (b) TC-5 position (Case 3, 5 & 6: D_p=10 mm; $\dot{V}_f$=1.5 L min^{-1}; charging).

$$f_r = \max\left[\left|\frac{\Delta T(t)}{T_H - T_C}\right|\right] = \max\left[\left|\frac{T^C(r,z,t) - \{T^B(r,z,t)\,,\,T^A(r,z,t)\}}{T_H - T_C}\right|\right] \quad (12)$$

The influence of radial thermocline expansion or instability due to the penetrating jet on the global performance of the SHTPB tank needs further discussion. To this end, **Fig. 11a** shows the energy efficiency (η_{ch}) and capacity ratio or utilization (C_{ratio}) at the cutoff time for different inlet configurations. For all studied inlet configurations, when T_H increases, the η_{ch} slightly decreases mainly

due to the higher heat loss, while the C_{ratio} slightly increases because of the larger temperature difference, which will be discussed in detail in the next subsection.

Case 5 with the most uniform radial temperature distribution at the inlet region has the largest capacity ratio and the longest charging time. The near plug flow pattern and the flattened thermocline shape indicate the better utilization of the storage capacity (around 3%) of the SHTPB tank. However, it presents the lowest energy efficiency (**Fig. 11a**) mainly due to the longest charging time before reaching the cutoff fluid outlet temperature thus the additional amount of heat loss as shown in **Fig. 11b**. In reality, the η_{ch} curves for Case 3 with serious radial thermocline expansion and Case 5 are very close (<2%) during the charging operation (**Fig. 11b**). This implies that the radial temperature non-uniformity and the thermocline expansion near inlet region caused by the penetrating HTF inject may have negligible influence on the energy efficiency of the SHTPB tank. It actually depends largely on the cutoff temperature and the corresponding cutoff time. The energy efficiency and capacity ratio of Case 6 with full water HTF in the entrance (thereby larger volumetric heat capacity than that of glass) are very close to those for Case 3. The near-entrance region of the tank is less utilized due to the strong mixing of hot and cold fluids, such as in single-medium thermocline tanks [56].

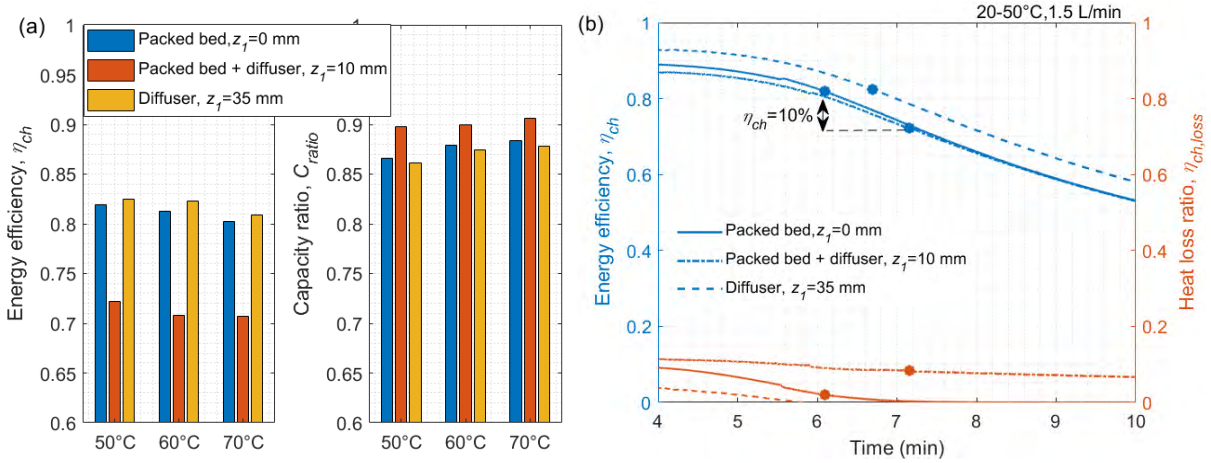

Fig. 11. Effect of inlet configuration on the global performance of the SHTPB tank: (a) energy efficiency and capacity ratio at cutoff time; (b) energy efficiency and heat loss ratio vs. charging time (Case 3, 5 & 6: D_p=10 mm, $\dot{V}_f$=1.5 L min^{-1}, charging).

Moreover, thermal infrared imaging is used on the tank outer surface to observe the qualitative trend of thermocline behavior . The wall emissivity is 0.90, the acquisition frequency is 0.1 Hz by using the Fluke thermal image camera TiS75 with a measuring range of -20 to 80 °C. **Fig. 12** shows the captured images for Case 5 without an insulation layer in charging and discharging operations. The thermocline region on the images is marked by dash line, showing that its thickness increases by 13 % from 2 min to 5 min in charging and discharging process. The flat shape of the thermocline region captured by infrared camera, may imply the good flow distribution behavior by the combined effect of porous bed and flow diffuser (Case 5).

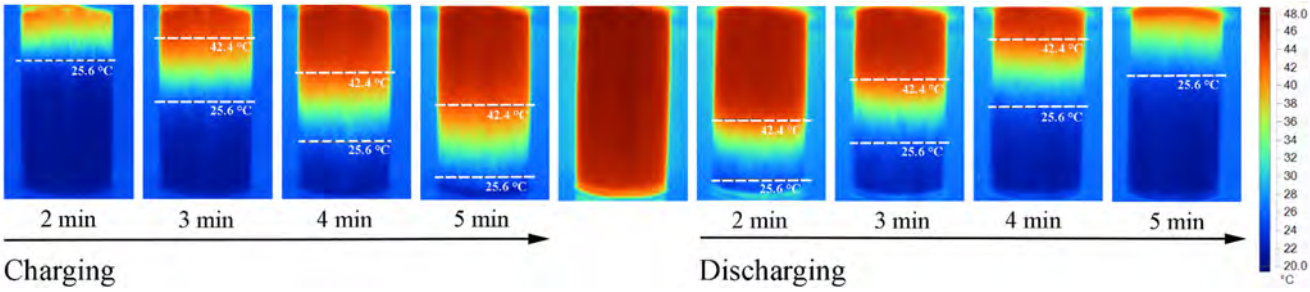

Fig. 12. Experimental thermal infrared images of charging and discharging process (T_C/T_H=20/50 °C, D_p=10 mm, 1.5 L min^{-1}, diffuser z_1=10 mm, no insulation, ϵ=0.90, T_{amb}=20.7 °C).

5.2.3. Impact of insulation

The impact of heat loss on the performance of the SHTPB tank has been evaluated by comparing the experimental results of Case 3 (with insulation) and Case 4 (without insulation) with the same testing condition. From **Fig. 13a**, it is found that due to the heat loss, the outlet fluid temperature of no-insulation tank is 5 ° C lower than that of the tank with insulation at the ending moment of charging (40 min, t*=2.5). Longer charging time of around 5% is also needed to reach the cutoff temperature (θ=0.2) when the tank is not insulated due to the serious tailing effect. **Fig. 13b** shows the variation of the normalized thermocline thickness over charging time for the two cases. It may be observed that the dimensionless thermocline thickness $L^*_{thermocline}$ values are almost the same before t*=0.34 (11 minutes) for the two cases. That is because, at the beginning of charging, the thermocline expansion at axial centerline is caused by fluid mixing and diffusion primarily. The near-wall region of the SHTPB tank is still occupied

by low-temperature HTF (cf. **Fig. 9a**) thus the influence of heat loss on the thermocline expansion is negligible. But at the second half of the charging, there is an obvious discrepancy between the two $L^*_{thermocline}$ curves, implying the noticeable influence of heat loss on the thermocline expansion. Comparing the insulation tank and no-insulation tank, the $L^*_{thermocline}$ is calculated to be 0.59 and 0.76 at t^*=1.38 (thermocline zone reaching the tank bottom).

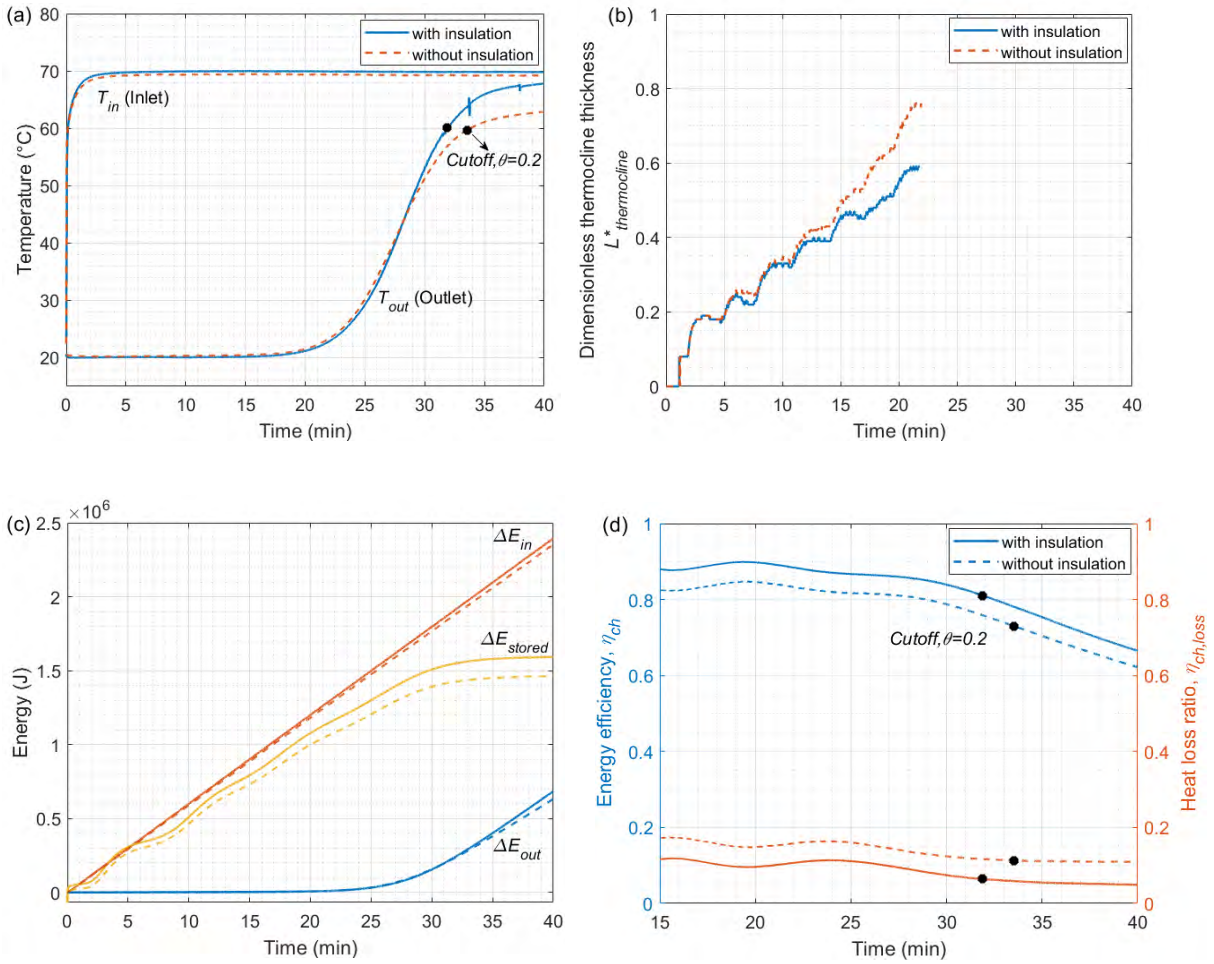

Fig. 13. Experimental results comparing the performance of SHTPB tank with/without insulation. (a) inlet and outlet temperature; (b) dimensionless thermocline thickness $L^*_{thermocline}$; (c) inlet/outlet and stored energy; (d) energy efficiency and heat loss ratio (Case 3 & 4: T_C/T_H=20/70 °C, D_p=10 mm, $\dot{V}_f$=0.3 L min^{-1}, θ=0.2).

Fig. 13c shows the variation of input energy (ΔE_{in}), stored energy (ΔE_{stored}), and outlet energy (ΔE_{out}) as a function of charging time for the SHTPB tank with/without the insulation. It is observed that both E_{stored} curves increase almost linearly until reaching a plateau. At the cutoff moment of charging, the E_{stored} value of no-insulation tank is 4-7% lower than that of the tank with insulation, mainly due to the heat loss. **Fig. 13d** shows the energy efficiency (η_{ch}) curve and heat loss ratio ($\eta_{ch,loss}$) curve, not surprisingly both indicating that the SHTPB tank performs better when well-insulated. At the cutoff temperature set as θ=0.2, the SHTPB tank with insulation can improve the energy efficiency by about 5-7%, increase total stored energy by 4-7%, and augment the capacity ratio by about 3-5%.

At last, the impacts of flow rates and inlet temperature with particle sizes on the thermocline evolution in axial direction further investigated experimentally are presented in Supplementary Material. When the HTF flow rate increases, the fluid temperature at the same height becomes higher because of the insufficient heat exchange (in Section S4, in Fig. S5). The thermocline thickness also increases faster at high HTF low rate (high Re) (in Section S4, in Fig. S6). Numerically, the smaller filler particle size is more advantageous and an optimal inlet flow rate (about Re=3) in charging can be identified for this SHTPB under low-temperature operation (in Section S5, in Fig. S7).

6. Conclusions

In this work, the impacts of inlet configuration and insulation on thermocline behavior and global performance of the SHTPB storage tank were investigated. The temperature evolution of both fluid and solid phases at different axial and radial positions of a lab-scale storage tank was experimentally measured. In parallel, a DC-3P numerical model has been developed and compared with the experimental data under various operating conditions. Main conclusions are summarized as follows.

(1) The developed DC-3P model considering the wall heat capacity and heat loss is proved to be able to predict the global performance precisely. Compared to the experimental data, the temperature standard deviation and energy efficiency difference can be kept below 2.5 °C and within 3%, respectively, under the applicable range of Re<15 and Bi_s<1.3.

(2) Temperature gradient inside spherical particle is shown to be existing due to the conduction resistance of the solid particles. A temperature difference up to 1.7 °C between the particle center and fluid has been observed both numerically and experimentally under our tested conditions.

(3) Injecting fluid in packed bed causes the non-uniform radial temperature distribution and thermocline expansion near the inlet region, especially at higher flow rate (higher *Re*). The combined effect of diffuser and packed bed as inlet configuration can better maintain the radial temperature uniformity as well as the thermocline stability. Nevertheless, the impact of injecting fluid on the global thermal performance of the tested SHTPB tank is rather limited.

(4) The heat loss without insulation layer could result in a noticeable thermocline expansion (>20%), lowered charging energy efficiency (5-7%), increased cutoff time (4-5%), and decreased capacity ratio (3-5%), even for low-temperature applications of the SHTPB storage tank.

This work can contribute to exploring the influencing factors based on a packing configuration by sensible fillers, enabling the inclusion of thermocline expansion into the design and optimization of low-temperature thermocline packed-bed system. Our on-going work is focused on the understanding and optimization of multi-layered packing configuration, using diverse phase change materials (PCMs) or mixtures of PCM-sensible material as fillers for different applications

Acknowledgements

This work is supported by the French ANR within the project OPTICLINE (ANR-17-CE06–0013) and by the Chinese Scholarship Council (CSC) with the scholarship for Ms. Baoshan XIE (No. 201908430177). Technical supports from Mr. Julien AUBRIL, Mr. Arnaud ARRIVE and Mr. Jorge FERNANDEZ-PACHECO ARMENTEROS during the experiments are gratefully appreciated.

References

[1] Internatioanl Energy Agency. Global Energy Review (report) 2022:[accessed 27 April 2022]. https://www.iea.org/.

[2] Kocak B, Paksoy H. Performance of laboratory scale packed-bed thermal energy storage using new demolition waste based sensible heat materials for industrial solar applications. *Sol Energy* 2020;211:1335–46.

[3] European Commission (EU). Renewable Energy 2022:[accessed 27 April 2022]. https://energy.ec.europa.eu/topics/renewable-energy_en.

[4] Khor JO, Yang L, Akhmetov B, Leal AB, Romagnoli A. Application of granular materials for void space reduction within packed bed thermal energy storage system filled with macro-encapsulated phase change materials. *Energy Convers Manag* 2020;222:113118.

[5] Xie B, Baudin N, Soto J, Fan Y, Luo L. Renewable Energy Production and Distribution: Recent Developments, Solutions and Opportunities, Chapter 10: Thermocline packed bed thermal energy storage system: a review. In: Mejdi Jeguirim, editor. Elsevier, 2022.

[6] Palomba V, Frazzica A. Application of numerical methods for the design of thermocline thermal energy storage: Literature review and critical analysis. *J Energy Storage* 2022;46:103875.

[7] Pelay U, Luo L, Fan Y, Stitou D, Rood M. Thermal energy storage systems for concentrated solar power plants. *Renew Sustain Energy Rev* 2017;79:82–100.

[8] Gautam A, Saini RP. A review on sensible heat based packed bed solar thermal energy storage system for low temperature applications. *Sol Energy* 2020;207:937–56.

[9] Soto J, Jadal M, de Guyenro N, Delaunay D. Thermal cycling aging of encapsulated phase change material – Compressed expanded natural graphite composite. *Therm Sci Eng Prog* 2021;22:100836.

[10] Pelay U, Luo L, Fan Y, Stitou D, Castelain C. Integration of a thermochemical energy storage system in a Rankine cycle driven by concentrating solar power: Energy and exergy analyses. *Energy* 2019;167:498–510.

[11] Lou W, Luo L, Hua Y, Fan Y, Du Z. A review on the performance indicators and influencing factors for the thermocline thermal energy storage systems. *Energies* 2021;14:8384.

[12] Rodrigues FA, de Lemos MJS. Effect of porous material properties on thermal efficiencies of a thermocline storage tank. *Appl Therm Eng* 2020;173:115194.

[13] Le Roux D, Lalau Y, Rebouillat B, Neveu P, Olivès R. Thermocline thermal energy storage optimisation combining exergy and life cycle assessment. *Energy Convers Manag* 2021;248:114787.

[14] Rosen MA. The exergy of stratified thermal energy storages. *Sol Energy* 2001;71:173–85.

[15] Hoffmann JF, Fasquelle T, Goetz V, Py X. Experimental and numerical investigation of a thermocline thermal energy storage tank. *Appl Therm Eng* 2017;114:896–904.

[16] Davenne TRG, Garvey SD, Cardenas B, Rouse JP. Stability of packed bed thermoclines. *J Energy Storage* 2018;19:192–200.

[17] Geissbühler L, Mathur A, Mularczyk A, Haselbacher A. An assessment of thermocline-control methods for packed-bed thermal-energy storage in CSP plants, Part 2: Assessment strategy and results. *Sol Energy* 2019;178:351–64.

[18] Cascetta M, Serra F, Arena S, Casti E, Cau G, Puddu P. Experimental and numerical research activity on a packed bed TES system. *Energies* 2016;9:1–13.

[19] Nicolas LF, Falcoz Q, Pham Minh D, Hoffmann JF, Meffre A, Nzihou A, et al. Flexibility and robustness of a high-temperature air/ceramic thermocline heat storage pilot. *J Energy Storage* 2019;21:393–404.

[20] Sanderson TM, Cunningham GT. Performance and efficient design of packed bed thermal storage systems. Part 1. *Appl Energy* 1995;50:119–32.

[21] Bruch A, Fourmigué JF, Couturier R. Experimental and numerical investigation of a pilot-scale thermal oil packed bed thermal storage system for CSP power plant. *Sol Energy* 2014;105:116–25.

[22] Yin H, Ding J, Yang X. Experimental research on thermal characteristics of a hybrid thermocline heat storage system. *Appl Therm Eng* 2014;62:293–301.

[23] Yin H, Ding J, Jiang R, Yang X. Thermocline characteristics of molten-salt thermal energy storage in porous packed-bed tank. *Appl Therm Eng* 2017;110:855–63.

[24] Reddy KS, Pradeep N. Stability analysis of the thermocline thermal energy storage system during high flow rates for solar process heating applications. *Sol Energy* 2021;226:40–53.

[25] Wang L, Yang Z, Duan Y. Influence of flow distribution on the thermal performance of dual-media thermocline energy storage systems. *Appl Energy* 2015;142:283–92.

[26] Vannerem S, Neveu P, Falcoz Q. Experimental and numerical investigation of the impact of operating conditions on thermocline storage performance. *Renew Energy* 2021;168:234–46.

[27] Cascetta M, Cau G, Puddu P, Serra F. Experimental investigation of a packed bed thermal energy storage system. J Phys Conf Ser 2015; 655:012018.

[28] Cascetta M, Serra F, Cau G, Puddu P. Comparison between experimental and numerical results of a packed-bed thermal energy storage system in continuous operation. *Energy Procedia* 2018;148:234–41.

[29] Cascetta M, Cau G, Puddu P, Serra F. A study of a packed-bed thermal energy storage device: Test rig, experimental and numerical results. *Energy Procedia* 2015;81:987–94.

[30] Hoffmann JF, Fasquelle T, Goetz V, Py X. A thermocline thermal energy storage system with filler materials for concentrated solar power plants: Experimental data and numerical model sensitivity to different experimental tank scales. *Appl Therm Eng* 2016;100:753–61.

[31] Xie B, Baudin N, Soto J, Fan Y, Luo L. Wall impact on efficiency of packed-bed thermocline thermal energy storage system. *Energy* 2022;247:123503.

[32] Douglas M. 10 MWe solar thermal central receiver pilot plant mode 5 (test 1150) and mode 6 (test 1160) test report. *Sandia Natl Lab SAND86-8175* 1986.

[33] Meier A, Winkler C, Wuillemin D. Experiment for modelling high temperature rock bed storage. *Sol Energy Mater* 1991;24:255–64.

[34] Pacheco J, Showalter S. Development of a molten-salt thermocline thermal storage system for parabolic trough plants. *J Sol Energy Eng* 2002;124:153–9.

[35] Yang X, Yang X, Ding J, Shao Y, Qin FGF, Jiang R. Criteria for performance improvement of a molten salt thermocline storage system. *Appl Therm Eng* 2012;48:24–31.

[36] Anderson R, Shiri S, Bindra H, Morris JF. Experimental results and modeling of energy storage and recovery in a packed bed of alumina particles. *Appl Energy* 2014;119:521–9.

[37] Al-Azawii MMS, Theade C, Danczyk M, Johnson E, Anderson R. Experimental study on the cyclic behavior of thermal energy storage in an air-alumina packed bed. *J Energy Storage* 2018;18:239–49.

[38] Al-Azawii MMS, Theade C, Bueno P, Anderson R. Experimental study of layered thermal energy storage in an air-alumina packed bed using axial pipe injections. *Appl Energy* 2019;249:409–22.

[39] Tuttle JF, White N, Mohammadi K, Powell K. A novel dynamic simulation methodology for high temperature packed-bed thermal energy storage with experimental validation. *Sustain Energy Technol Assessments* 2020;42:100888.

[40] Keilany MA, Milhé M, Bézian JJ, Falcoz Q, Flamant G. Experimental evaluation of vitrified waste as solid fillers used in thermocline thermal energy storage with parametric analysis. *J Energy Storage* 2020;29:101285.

[41] Vannerem S, Neveu P, Falcoz Q. Experimental investigation of the impact of fluid distribution on thermocline storage performance. *J Energy Storage* 2022;52:104864.

[42] Gautam A, Saini RP. Development of correlations for Nusselt number and friction factor of packed bed

solar thermal energy storage system having spheres with pores as packing elements. *J Energy Storage* 2021;36:102362.

[43] Bruch A, Bourdon D, Dumas C, Blaise A, Chouvel-Saye A. Experimental characterization of a water/rock thermocline cold thermal energy storage for optimization of condenser cooling. *J Energy Storage* 2021;44:103426.

[44] Alonso E, Rojas E. Air solid packed-beds for high temperature thermal storage: practical recommendations for predicting their thermal behaviour. *Appl Therm Eng* 2022;202:117835.

[45] Xu C, Liu M, Jiao S, Tang H, Yan J. Experimental study and analytical modeling on the thermocline hot water storage tank with radial plate-type diffuser. *Int J Heat Mass Transf* 2022;186:122478.

[46] Lai Z, Zhou H, Zhou M, Lv L, Meng H, Cen K. Experimental study on storage performance of packed bed solar thermal energy storage system using sintered ore particles. *Sol Energy Mater Sol Cells* 2022;238:111654.

[47] Lou, W., Xie, B., Aubril, J., Fan, Y., Luo, L. AA. Optimized flow distributor for stabilized thermal stratification in a single-medium thermocline storage tank: A numerical and experimental study. *Energy* 2023;263:125709.

[48] Esence T, Bruch A, Molina S, Stutz B, Fourmigué JF. A review on experience feedback and numerical modeling of packed-bed thermal energy storage systems. *Sol Energy* 2017;153:628–54.

[49] Rady M. Thermal performance of packed bed thermal energy storage units using multiple granular phase change composites. *Appl Energy* 2009;86:2704–20.

[50] Fasquelle T, Falcoz Q, Neveu P, Hoffmann JF. A temperature threshold evaluation for thermocline energy storage in concentrated solar power plants. *Appl Energy* 2018;212:1153–64.

[51] Abdulla A, Reddy KS. Effect of operating parameters on thermal performance of molten salt packed-bed thermocline thermal energy storage system for concentrating solar power plants. *Int J Therm Sci* 2017;121:30–44.

[52] Cocco D, Serra F. Performance comparison of two-tank direct and thermocline thermal energy storage systems for 1MWe class concentrating solar power plants. *Energy* 2015;81:526–36.

[53] Modi A, Pérez-Segarra CD. Thermocline thermal storage systems for concentrated solar power plants: One-dimensional numerical model and comparative analysis. *Sol Energy* 2014;100:84–93.

[54] Chang Z, Li X, Xu C, Chang C, Wang Z. The design and numerical study of a 2 MWh molten salt thermocline tank. *Energy Procedia* 2015;69:779–89.

[55] Hänchen M, Brückner S, Steinfeld A. High-temperature thermal storage using a packed bed of rocks - Heat transfer analysis and experimental validation. *Appl Therm Eng* 2011;312:1798–806.

[56] Lou W, Fan Y, Luo L. Single-tank thermal energy storage systems for concentrated solar power: Flow distribution optimization for thermocline evolution management. *J Energy Storage* 2020;32:101749.

[57] Taylor BN, Kuyatt CE. Guidelines for evaluating and expressing the uncertainty of NIST measurement results. 1994.

[58] Stern F, Muste M, Beninati M, Eichinger WE. Summary of exerimental uncertainty assessmet methodology. 1999.

[59] Wang W, He X, Hou Y, Qiu J, Han D, Shuai Y. Thermal performance analysis of packed-bed thermal energy storage with radial gradient arrangement for phase change materials. *Renew Energy* 2021;173:768–80.

Experimental and numerical study on the thermocline behavior of packed-bed storage tank with sensible fillers

Baoshan XIE[a], Nicolas BAUDIN[a], Jérôme SOTO[a,b], Yilin FAN[a], Lingai LUO[a,1]

[a] *Nantes Université, CNRS, Laboratoire de Thermique et énergie de Nantes, LTeN, UMR 6607, 44000 Nantes, France*

[b] *Institut Catholique d'Arts et Métiers de Nantes, 35 avenue du Champ de Manœuvres, 44470 Carquefou, France*

Supplementary Material

[1] Corresponding author

E-mail address: lingai.luo@univ-nantes.fr (L. LUO)

S1. Solving

The equations presented above were discretized by the explicit Runge Kutta (4.5) method with an adaptive time step. The model was solved with the MATLAB function ode45 for the time derivatives. **Fig. S1** shows the results of height mesh size and time step sensibility test with a variation of the particle mesh size. It calculated that the cutoff temperature variation is smaller than 1% when the height node number ($N = \frac{H}{\Delta z}$) and time node number ($M = \frac{t}{\Delta t}$) is larger than 1000, with an increase of particle radius node number ($F = \frac{D_p}{\Delta r_p}$) from 5 to 20. The particle node has a minor influence on the convergence of cutoff temperature. Thus, N=1000 and M=1000 are used for height and time node differential mesh, respectively, and F=20 is chosen to better capture the temperature gradient inside the particle.

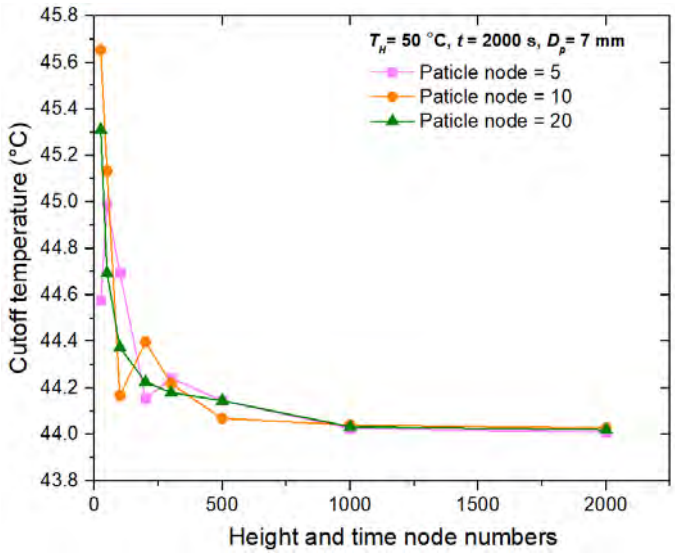

Fig. S1. Height, time, and particle radius node number independence tests in differential mesh.

S2. Calibrating experiment measurement

The thermocouples were calibrated with an oil FLUKE 6102 MICRO-BATH calibration device in the validation range of 35-200 °C and by the low-temperature thermostat below 35 °C. The specific heat capacity of glass sphere was measured by Differential Scanning Calorimetry (DSC Q200) with a heating/cooling rate of 5 K min^{-1} showing in **Fig. S2a**. It was obtained that both thermophysical properties are the same. The inlet flow rate was calibrated by the gravimetric method with testing curves shown in **Fig. S2b**. The thermal conductivity of insulation was measured by Thermal Constants Analyser (Hot-Disk TPS1500) at different temperatures, with a small variation rate of 2.7×10^{-3} W m^{-1} K^{-1} per 1 K shown in **Fig. S2c**.

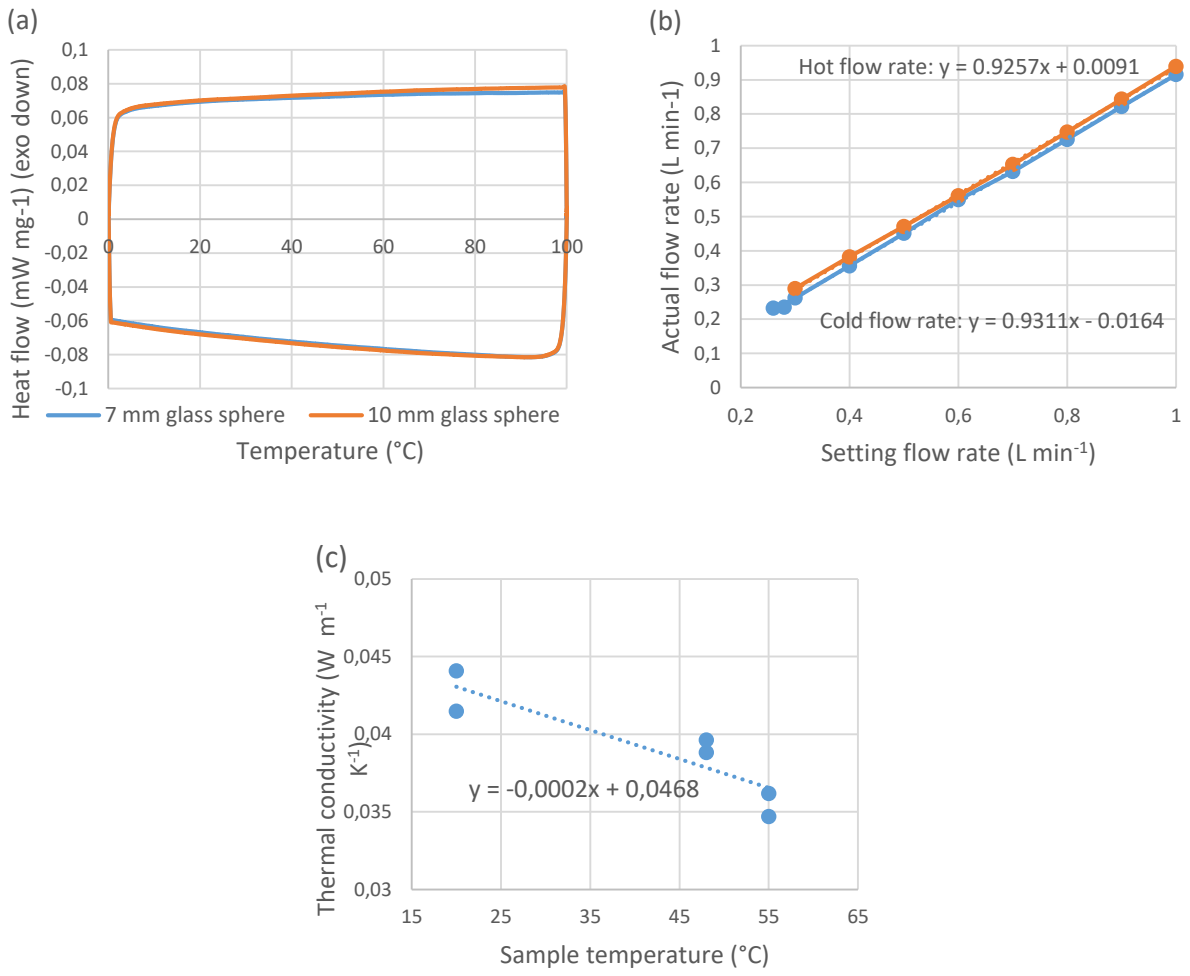

Fig. S2. (a) Differential scanning calorimetry curves of glass sphere in range of 0-100 °C; (b) Calibrated flow rates of hot and cold water; (c) Measured thermal conductivity of insulation with temperature increase.

The hot flow rate (L min^{-1}) is calibrated into:

$$\dot{V}_f(Actual) = \dot{V}_f(setting) \cdot 0.9257 + 0.0091.$$

The cold flow rate (L min^{-1}) is calibrated into:

$$\dot{V}_f(Actual) = \dot{V}_f(setting) \cdot 0.9311 - 0.0164.$$

S3. Uncertainty analysis

The measurement uncertainties were obtained by evaluating the standard deviation in repeated testing [1]. The analytical uncertainties for in-direct parameters, such as energy efficiency, are determined by the components uncertainties, ϑ, that are contributed by the measurement uncertainties based on error propagation [2]. In experiment, the average temperature of small unit volume is used to calculate energy. Both measurement uncertainty and analytic interpolation integral uncertainty of the average temperature can influence the energy calculation (average temperature is actually a type of middle point integration method). Firstly, the temperature error (systematic error) is estimated to be ±0.37 K, the measurement uncertainty on average temperature is calculated to be ±0.15 °C, and the numerical integration uncertainty is below that, as calculated in **Fig. S3a**. Especially due to the different radial thermocouples number, the uncertainty is different for radial thermocouples. Thus, among those, system error of ±0.37 K is used to calculate the in-direct parameters uncertainty. The corresponding uncertainty of stored energy, input energy, and efficiency of the validation case are exhibited in **Fig. S3 b-d**.

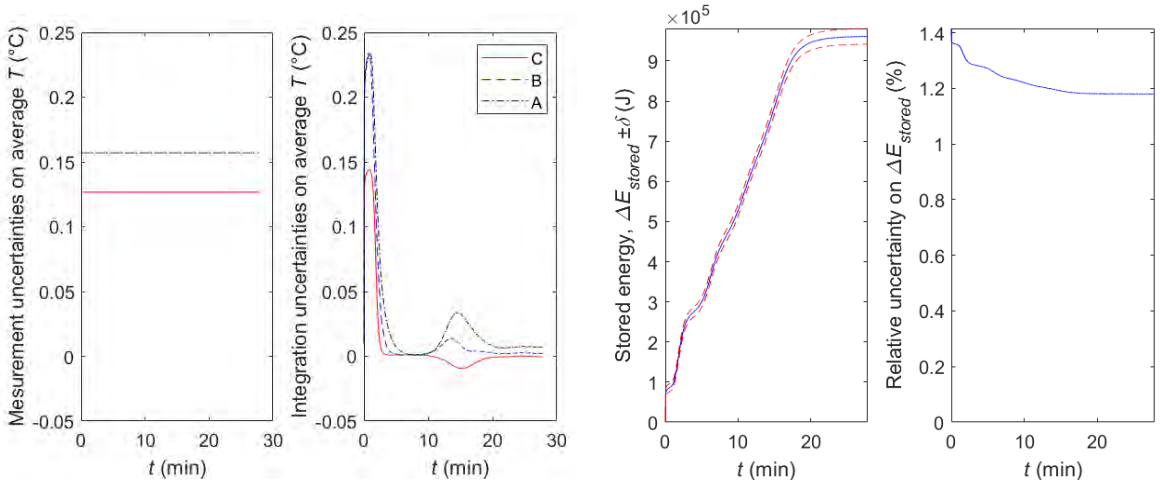

(a) (b)

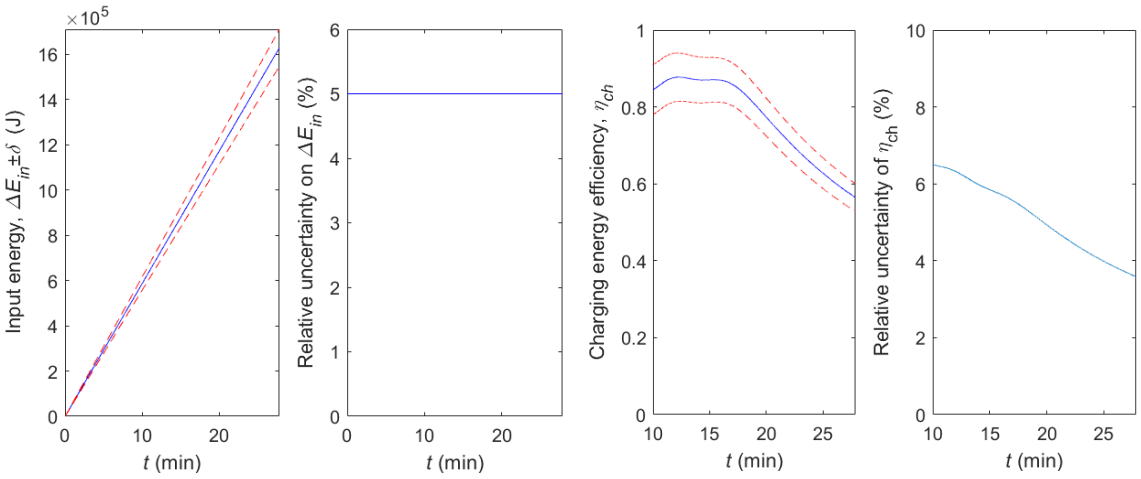

(c) (d)

Fig. S3. Uncertainty of the validation case: (a) bed average temperature; (b) stored energy (E_{stored}) based on bed average temperature; (c) input energy (E_{in}) based on bed average temperature; (d) energy efficiency (η_{ch}) based on bed average temperature.

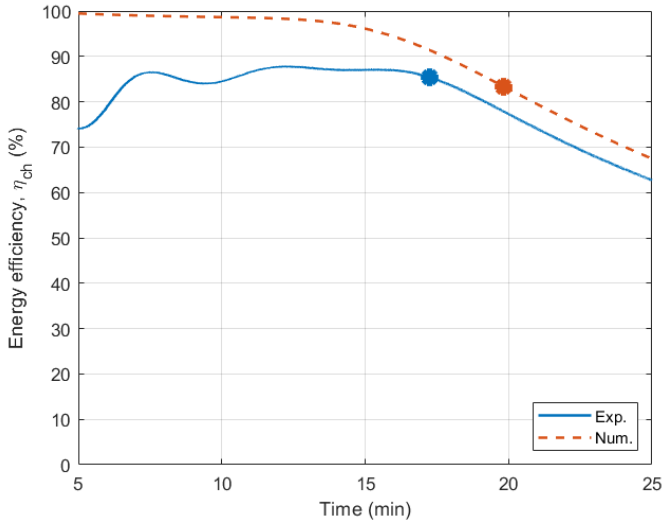

Fig. S4. Energy efficiency comparison for numerical and experimental in charging process (T_C/T_H=20/50 °C, D_p=7 mm, $\dot{V}_f$ =0.5 L min^{-1}).

S4. Impact of flow rates and inlet HTF temperature

The influence of HTF flow rate and inlet temperature on the thermocline evolution in axial direction is further investigated experimentally and reported in this sub-section. **Fig. S5** shows the fluid temperature profile along the tank height (centerline) for various flow rates, particles size, and operating temperatures at charging time of t_E^*=0.5 (input energy by HTF is equal to the half of ideal maximum stored energy of tank). When HTF flow rate increases from 0.3 to 1.5 L min^{-1} and the theoretical input energy by HTF is the same, the fluid temperature at the same z^* becomes higher. That's because the shorter residence time at higher flow rate causes insufficient heat exchange between solid and HTF.

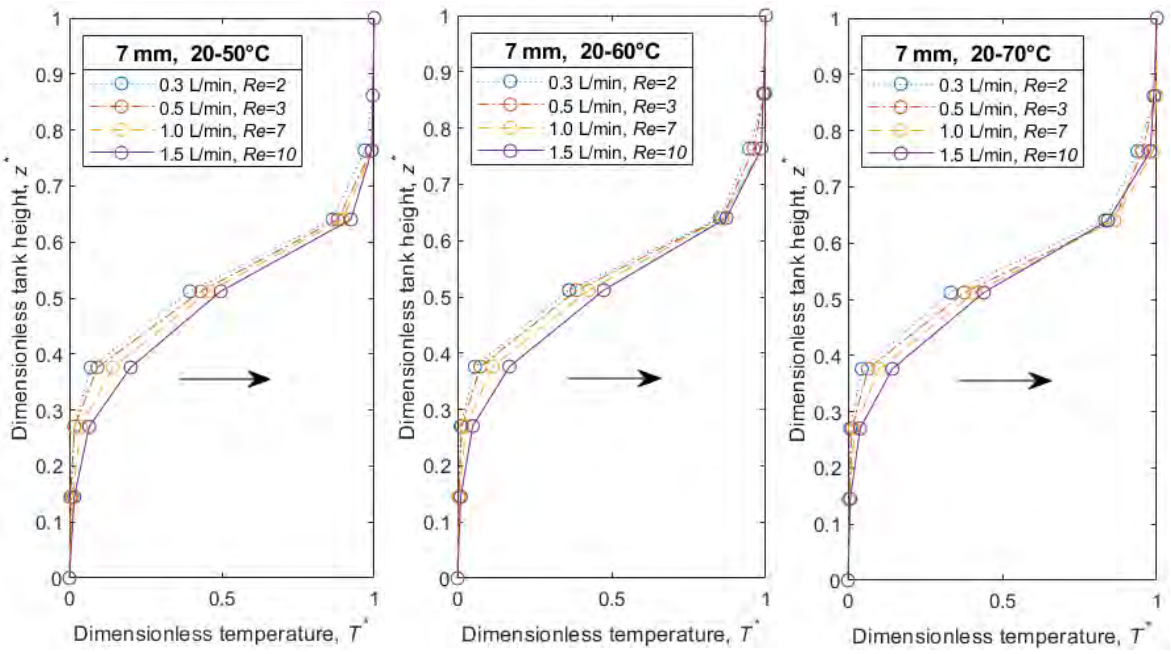

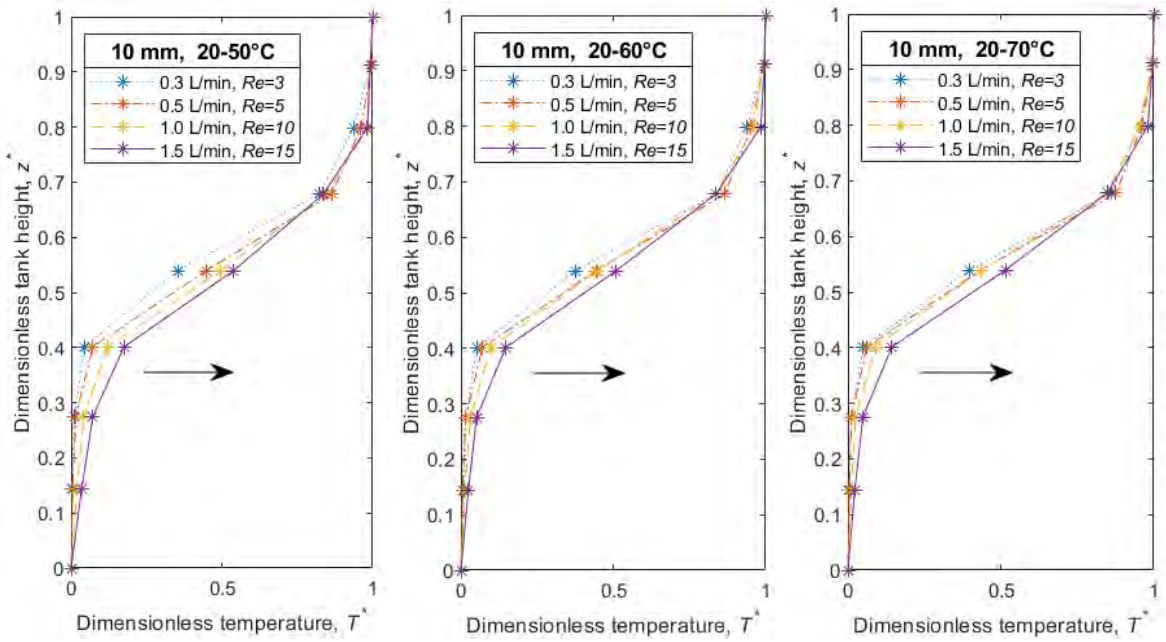

Fig. S5. Experimental fluid temperature profile at the axial centerline of the SHTPB tank for various flow rates, particles sizes, and working temperatures at charging time of t_E^*=0.5.

Fig. S6 shows the variation of normalized thermocline thickness as a function of t_E^* in charging. Curves are fitted linearly for a better comparison using the direct proportion formula, $L^* = k \cdot t_E^*$, and the slope value k for each curve is indicated aside. The thermocline expands over time due to various factors discussed before and its thickness can go up to 70% of the total tank height. From **Fig. S6** it can be observed that the thermocline thickness increases faster at high HTF rate (high Re). Whether there is an optimum flow rate value at very low Re condition will be discussed later. In addition, the slope value becomes a bit smaller with increasing T_H under the same flow rate. This is because the higher inlet fluid temperature augments the fluid-solid heat transfer rate, thereby slowing the thermocline expansion.

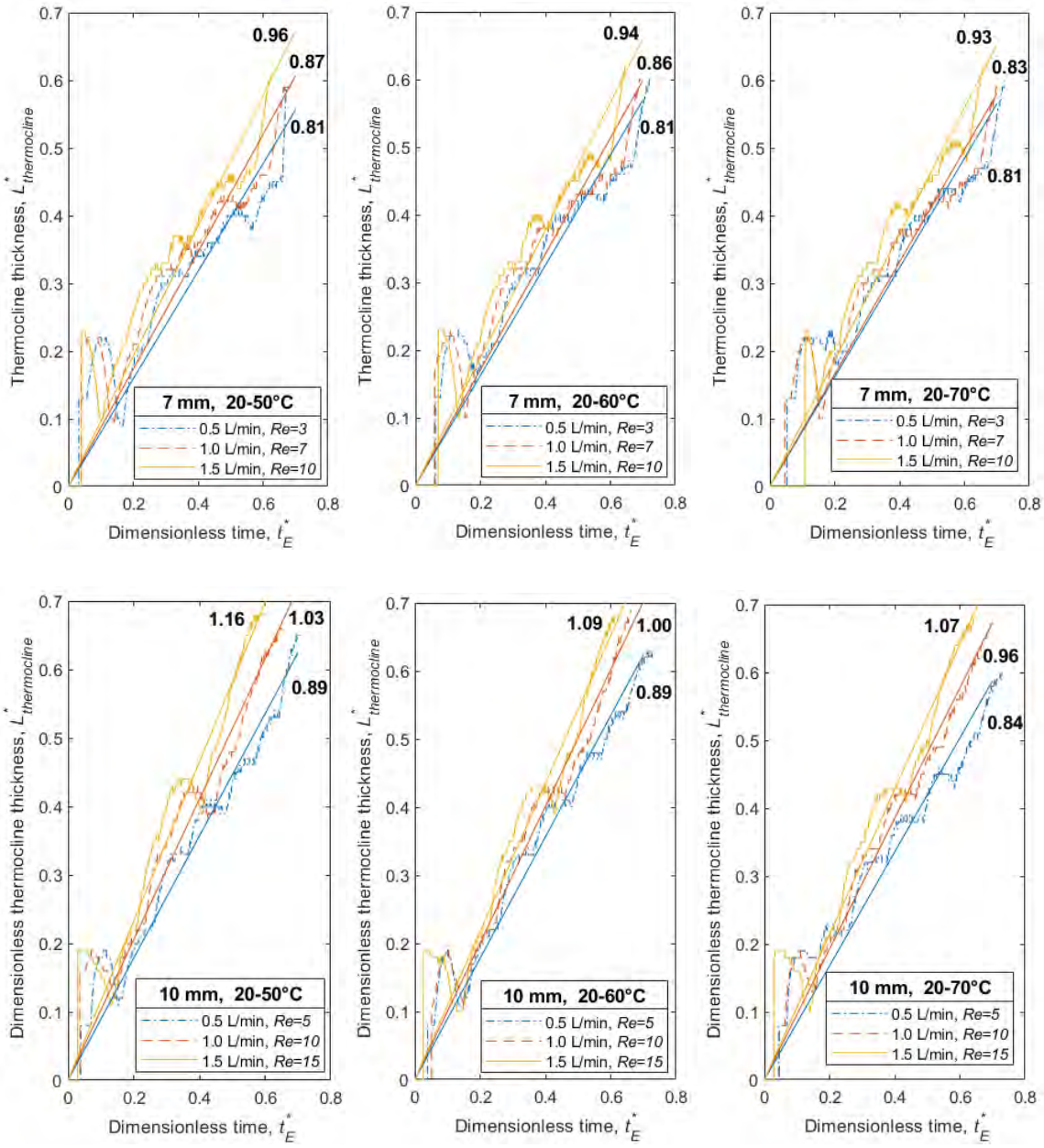

Fig. S6. Evolution of thermocline thickness for various flow rates, particles sizes, and working temperatures in charging process.

S5. Optimal flow velocity

Additional simulations using the DC-3P model have been performed and compared with the experimental data in order to exhibit the existence (or not) of an optimal HTF flow rate (Re) for SHTPB TES tanks. **Fig. S7** shows the numerical results of the energy efficiency and remained thermocline thickness at cutoff time with HTF flow rate ranging from 0.12 to 2.5 L min^{-1} (Re=0.8-25). The inlet fluid temperature has negligible effect on the energy efficiency and the remained thermocline thickness. Numerically, the smaller filler particle size is more advantageous and an optimal inlet flow rate (about Re=3) in charging can be identified for this SHTPB under low temperature operation. This finding is in line with other researches for high- or middle- temperature applications [3][4][5]. Unfortunately, this optimum is not significant enough to be detected in experiments. One reason is due to the stability of operations and measuring uncertainties. Another reason is caused by the regime in the change of flow behind obstacles or particles. When the HTF flow distance in the packed bed increases and when the mass flow rate increases, the heat transfer efficiency of the regime behind the particle thereby decreases, which cannot be simulated in the 1D fluid model in Matlab.

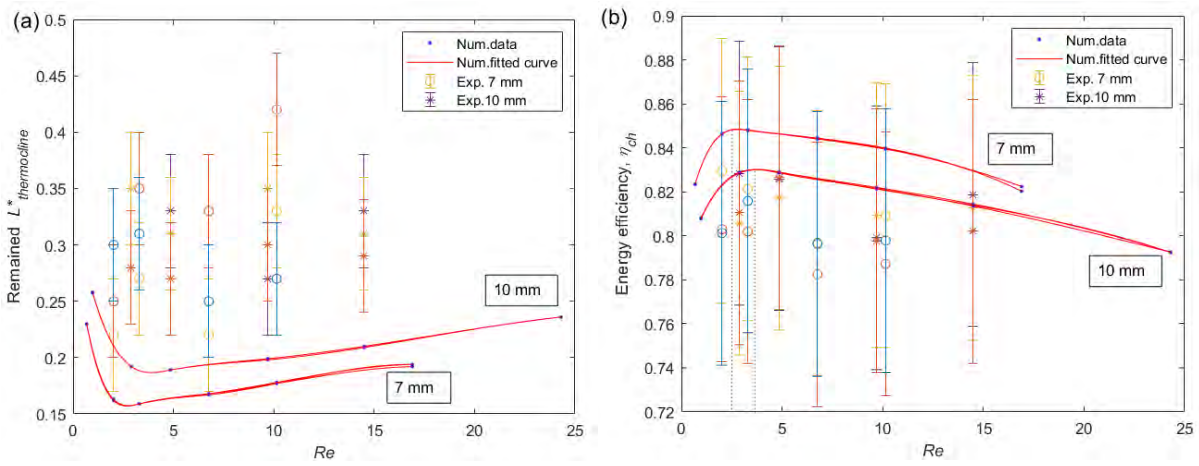

Fig. S7. Influence of flow velocity (Re) on energy efficiency and thermocline thickness: comparison between experiment and numerical results (T_H: 50-70 °C, $\dot{V}_f$=0.12-2.5 L min^{-1}).

References

[1] Taylor BN, Kuyatt CE. Guidelines for evaluating and expressing the uncertainty of NIST measurement results. Natl Inst Stand Technol Gaithersburg, MD 2001:D.1.1.2.

[2] He Z, Wang X, Du X, Amjad M, Yang L, Xu C. Experiments on comparative performance of water thermocline storage tank with and without encapsulated paraffin wax packed bed. Appl Therm Eng 2019;147:188–97.

[3] Kocak B, Paksoy H. Performance of laboratory scale packed-bed thermal energy storage using new demolition waste based sensible heat materials for industrial solar applications. Sol Energy 2020;211:1335–46.

[4] Hoffmann JF, Fasquelle T, Goetz V, Py X. Experimental and numerical investigation of a thermocline thermal energy storage tank. Appl Therm Eng 2017;114:896–904.

[5] Vannerem S, Neveu P, Falcoz Q. Experimental and numerical investigation of the impact of operating conditions on thermocline storage performance. Renew Energy 2021;168:234–46.